Geophys. J. Int. (1993) **115**, 878–904

Global mapping of upper mantle reflectors from long-period *SS* precursors

Peter M. Shearer

Institute of Geophysics and Planetary Physics, Scripps Institution of Oceanography, University of California, La Jolla, CA 92093–0225, *USA*

Accepted 1993 May 3. Received 1993 May 3; in original form 1992 December 14

SUMMARY

Long-period precursors to *SS* resulting from underside reflections off upper mantle discontinuities (*SdS* where *d* is the discontinuity depth) can be used to map the global distribution and depth of these reflectors. We analyse 5,884 long-period seismograms from the Global Digital Seismograph Network (1976–1987, shallow sources, transverse component) in order to identify *SdS* arrivals. Corrections for velocity dispersion, topography and crustal thickness at the *SS* bounce point, and lateral variation in mantle velocity are critical for obtaining accurate estimates of discontinuity depths. The 410 and 660 km discontinuities are observed at average depths of 413 and 653 km, and exhibit large-scale coherent patterns of topography with depth variations up to 40 km. These patterns are roughly correlated with recent tomographic models, with fast anomalies in the transition zone associated with highs in the 410 km discontinuity and lows in the 660 km discontinuity, a result consistent with laboratory measurements of Clapeyron slopes for the appropriate phase changes. The best resolved feature in these maps is a trough in the 660 km discontinuity in the northwest Pacific, which appears to be associated with the subduction zones in this region. Amplitude variations in *SdS* arrivals are not correlated with discontinuity depths and probably result from focusing and defocusing effects along the ray paths. The *SdS* arrivals suggest the presence of regional reflectors in the upper mantle above 400 km. However, only the strongest of these features are above probable noise levels due to sampling inadequacies.

Key words: mantle discontinuities, seismic reflectors, upper mantle.

INTRODUCTION

Seismologists have found evidence for discontinuities in the upper mantle at a variety of depths, but the significance of differences in these depths is not yet clear. Are these differences required by the data or could they be a result of different modeling assumptions? Do they describe global features or do they represent more regional velocity anomalies? Is there topography on the major discontinuities? How reliable are observations of reflectors outside the major discontinuities? Fig. 1 plots upper mantle discontinuity depths from observations given in 55 papers over the last 25 years (for the purposes of this plot and for the remainder of this paper, the term 'discontinuity' is used loosely to refer to either an abrupt velocity change or a steep velocity gradient). Although undoubtedly some authors have been left out of this compilation, the overall pattern is clear. Consistent evidence has been found for the well-known discontinuities near 410 and 660 km, but depths to these features have varied by 40 km or more. There have also been sporadic observations of discontinuities near 220 and 520 km, and occasional evidence for discontinuities at other depths as well, particularly in the region above the transition zone.

Traditional investigations of mantle discontinuities based on the techniques of refraction seismology have recently been supplemented by a wealth of new observations of secondary seismic phases caused by discontinuity reflections and phase conversions. Analyses of these phases using stacking and other reflection seismology methods are beginning to provide much more detailed images of discontinuity structure than were previously possible. Revenaugh & Jordan (1987, 1989, 1991a,b) pioneered the use of long-period *ScS* reverberations to study discontinuity structure and found significant variations in the depths to the 410 and 660 km discontinuities and identified numerous reflectors in addition to the major discontinuities. They found reflectors near 520, 710 and 900 km and at a wide

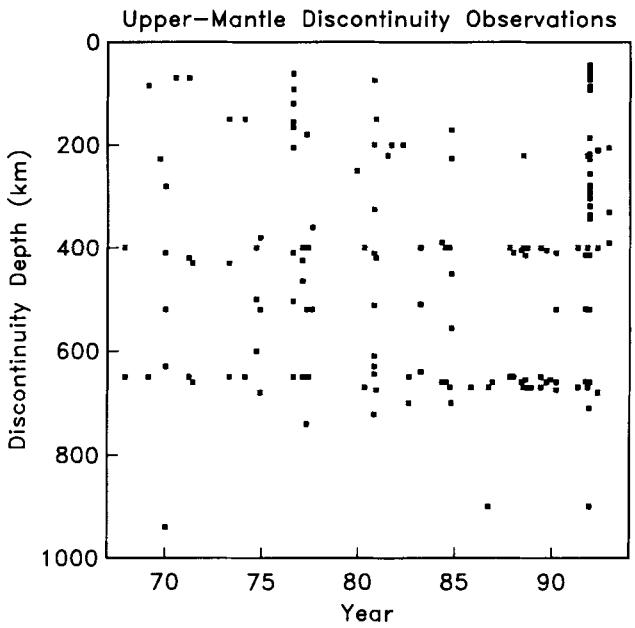

Figure 1. Upper mantle discontinuity observations from the last 25 years. Enhanced velocity gradients are treated as discontinuities for the purposes of this plot. Observations are from Adams (1971), Barley, Hudson & Douglas (1982), Baumgardt & Alexander (1984), Bock (1988), Bock & Ha (1984), Bock & Kind (1991), Davis, Kind & Sacks (1989), Dey-Sarker & Wiggins (1976), Drummond, Muirhead & Hales (1982), Dziewonski & Anderson (1981), Engdahl & Flinn (1969), Faber & Müller (1980, 1984), Fukao (1977), Given & Helmberger (1980), Grand & Helmberger (1984), Graves & Helmberger (1988), Gutowski & Kanasewich (1974), Hales (1969), Hales *et al.* (1980), Helmberger & Engen (1974), Helmberger & Wiggins (1971), Husebye, Maddon & King (1977), Johnson (1967), Kanamori & Press (1970), Kind & Vinnik (1988), LeFevre & Helmberger (1989), Leven, Jackson & Ringwood (1981), Nakanishi (1986, 1988, 1989), Niazi (1969), Nolet (1977), Paulssen (1985, 1988), Ram & Mereu (1977), Revenaugh & Jordan (1987, 1989, 1991a,b), Richards & Wicks (1990), Sacks, Snoke & Husebye (1979), Shearer (1990, 1991), Simpson, Merau & King (1974), Souriau (1986), Stammler *et al.* (1991), Vidale & Benz (1992), Vinnik (1977), Vinnik, Avetisjan & Mikhailova (1983), Walck (1984), Wallace & Holt (1988), Whitcomb & Anderson (1970), Wiggins & Helmberger (1973), and Zhang & Lay (1993).

range of depths above 400 km depending upon the region sampled.

Recent global stacks of long-period body wave data have confirmed the existence of discontinuities near 410, 520 and 660 km, but find no evidence for globally coherent discontinuities above 400 km (Shearer 1990, 1991). Long-period *SS* precursors have particularly good global coverage, and analyses of these phases have indicated large-scale topographic variations on the 410 and 660 km discontinuities with depth variations of about 30 km (Shearer 1991; Shearer & Masters 1992). This paper is concerned with the general problem of using *SS* precursors to map reflectors within the upper mantle. Goals of this research include producing maps of topography on the 410 and 660 km discontinuities and assessing the reliability of apparent observations of regional reflectors at other depths. This work is a continuation of previous analyses of long-period discontinuity phases (Shearer 1990, 1991; Shearer & Masters 1992) to which the reader is referred for additional details regarding some of the data and techniques. This paper describes more data and improved analysis methods compared to the previous work; these differences will be emphasized where appropriate.

PRECURSORS TO *SS*

Long-period precursors to *SS* which result from underside reflections off upper mantle discontinuities have the ray geometry shown in Fig. 2. Differential times between these phases and *SS* (i.e. *SS–SdS* where *d* is the discontinuity depth) provide a measure of the two-way *S* traveltime between the surface and the discontinuity. Structure near the sources and receivers is relatively unimportant since the *SS* and *SdS* ray paths are nearly identical except near the

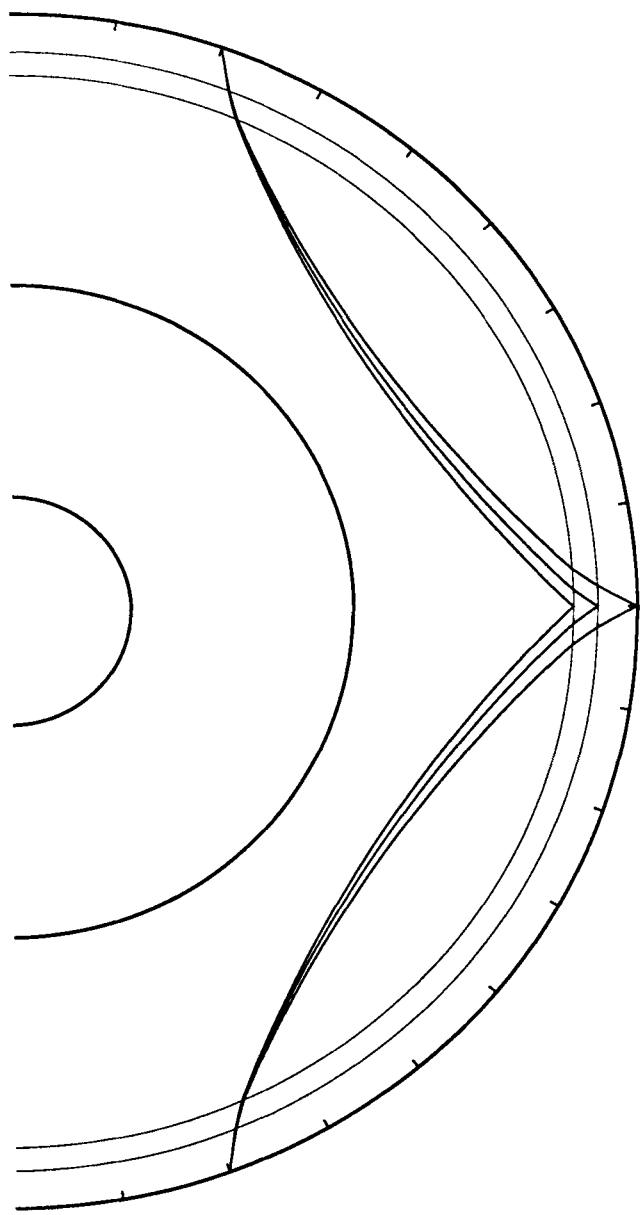

Figure 2. *SS*, $S_{410}S$ and $S_{660}S$ ray paths at 140° range plotted for the ISAPEI91 velocity model.

bounce points. Although long-period *SdS* arrivals can be imaged at ranges as close as 75°, they are seen most clearly between 110° and 180° where they do not overlap with the topside multiples following direct *S* (e.g. Shearer 1991). Our previous studies of *SdS* phases restricted the analysis to seismograms in which the amplitude of the *SS* arrival was at least five times larger than the preceding 'noise'. For Global Digital Seismograph Network (GDSN) data from 1976 to 1987, this limited the number of seismograms to 3,139 for shallow events (<75 km) at ranges between 110° and 180° (Shearer & Masters 1992).

We now explore the effect of changing this signal-to-noise cut-off for the *SS* arrivals to see if more data can be used. Fig. 3 is a smoothed histogram of apparent discontinuity depths obtained from seismograms of varying *SS* amplitude levels. *SdS* arrivals are identified by computing the cross-correlation function between the *SS* arrival and the remainder of the seismogram (see Shearer 1991, for details of this method). This procedure obtains traveltimes and amplitudes of possible *SdS* arrivals relative to the *SS* traveltime. Assuming an upper mantle velocity model, these times can be converted to apparent discontinuity depths. The histograms in Fig. 3 show the difference between the positively and negatively correlated apparent *SdS* arrivals; this is why each histogram has approximately zero mean. The 410 and 660 km discontinuities can be identified as peaks in these plots, even for *SS* arrivals with signal-to-noise ratios as low as 2 to 3. This suggests that much of the 'noise' preceding *SS* contains information about upper mantle reflectors, although the expected amplitude of *SdS* arrivals is typically less than 10 per cent of *SS* (e.g. Shearer 1991). It is interesting to note in Fig. 3 that although small peaks above 400 km appear on individual histograms, they are at varying depths for these different subsets of the waveforms. Only the peaks near 410, 520 and 660 km appear consistently throughout the data.

Subsequent analyses in this paper are restricted to seismograms with *SS* signal-to-noise ratios greater than 3. This results in 5,884 traces (GDSN 1976 to 1987, event depth < 75 km, 110° to 180° range), a significant increase in data over the 3,139 seismograms used in Shearer & Masters (1992). *SS* bounce-point locations for these traces are shown in Fig. 4. The bounce-point distribution provides reasonable global coverage for imaging upper mantle discontinuities.

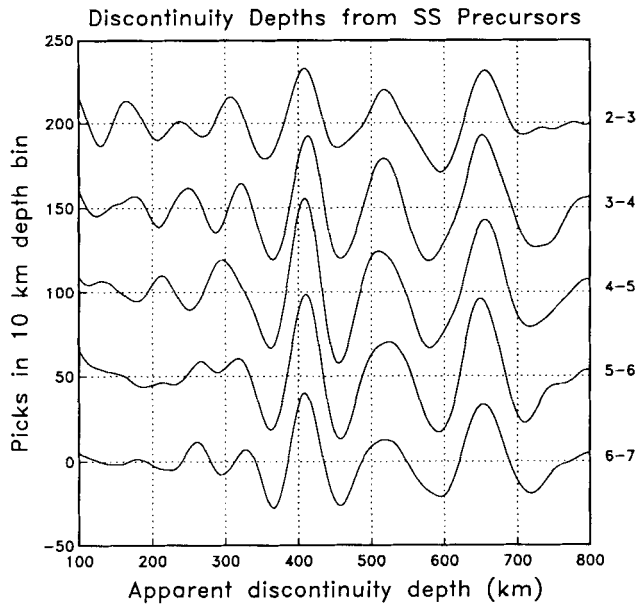

Figure 3. Histograms of apparent discontinuity depths for a range of *SS* signal-to-noise ratios. Each histogram shows the difference between the positively correlated picks and the negatively correlated picks in a 10 km depth bin and has been smoothed by a $\cos^2$ function of 30 km half-width. The range of *SS* signal-to-noise levels for each histogram is shown to the right; histograms are offset for clarity. Notice that the 410 and 660 km peaks can be seen at all *SS* signal levels considered.

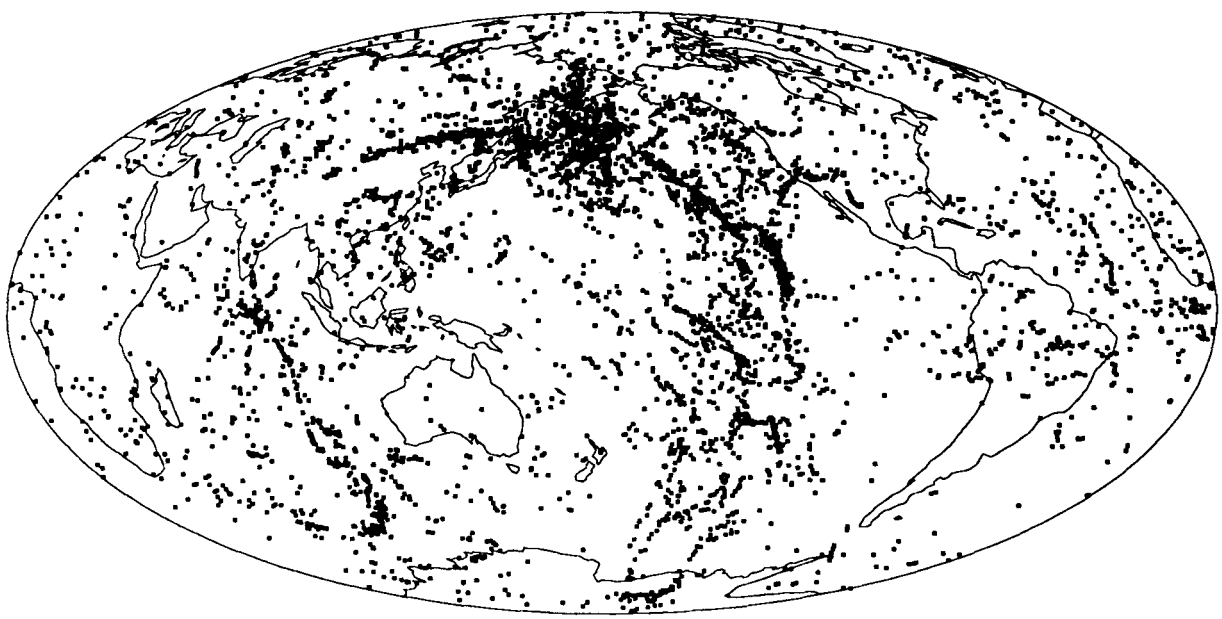

Figure 4. *SS* bounce-point locations for the 5,884 seismograms used in the analysis of *SdS* arrivals. Source–receiver ranges are between 110° and 180°.

This is a substantial advantage of *SS* precursors over most other discontinuity phases which generally image discontinuities only in regions near the sources and receivers. Coverage is especially good in the northwest Pacific, midway between earthquakes in the southwest Pacific and stations in Europe and North America.

CONVERSION FROM TIME TO DEPTH

SS–SdS arrival times obtained from these seismograms are converted to discontinuity depths by assuming a reference radial velocity model and applying corrections for lateral variations in mantle structure. In previous analyses this was done using PREM as the reference and *SS–S* times from Woodward & Masters (1991) to account for mantle heterogeneity. We have now improved this procedure to account more accurately for bounce-point topography and crustal thickness, dispersion, and current models of mantle *S*-wave structure.

The *SS–SdS* times are directly related to the two-way *S* traveltime between the surface and the discontinuity. The *S*-wave velocity at 410 and 660 km is about 4.8 and 5.7 km s^{-1}, respectively. Thus, a 2 s difference in two-way vertical traveltime will cause changes of roughly 5 to 6 km in depths to these discontinuities. Variations in the assumed radial reference model will directly affect the calculated discontinuity depths. Fig. 5 shows a comparison between integrated vertical *S* traveltimes for the isotropic PREM (Dziewonski & Anderson 1981) and IASPEI91 (Kennett 1991) models (the ocean in PREM has been filled in for this calculation). The differences between these models are generally very small, particularly below 400 km depth. For example, at 410 km the models agree within about 0.2 s, which would cause a change in the depth to the 410 km discontinuity of only about 1 km.

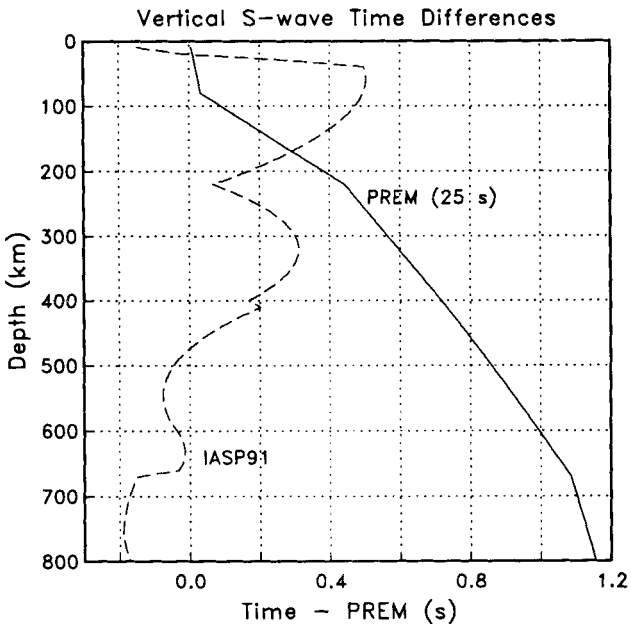

Figure 5. Vertical *S*-wave traveltimes relative to PREM (1 s) for IASPEI91 and PREM (25 s). The slightly slower velocities predicted by PREM at longer periods cause about a 1 s delay in *S*-wave traveltimes between the surface and 660 km.

However, it is important to remember that these models are for seismic energy at about 1 Hz, whereas the data used in this paper are at periods of about 25 s. Seismic velocities are reduced slightly at longer periods due to the effects of dispersion. PREM specifies Q as a function of depth, so velocities and traveltimes can be computed at arbitrary periods. Fig. 5 shows the difference between vertical traveltimes for PREM at 25 s compared to PREM at 1 s. This difference is much larger than the difference between IASPEI91 and the PREM at 1 Hz, and amounts to about 0.7 s at 400 km and 1.1 s at 650 km. Use of the 25 s PREM model will reduce the calculated average apparent depths to the 410 and 660 km discontinuities by roughly 3 km and 6 km, respectively. Previous analyses of *SS* precursors (Shearer 1991; Shearer & Masters 1992) assumed PREM at 1 Hz and thus did not properly account for velocity dispersion. Note that our new analysis does not attempt to account for the extra pulse broadening from attenuation in *SS* relative to *SdS*, but the use of the 25 s PREM model corrects to first order for the time shift between the t^* operators for these phases.

In order to obtain the best possible discontinuity depth estimates at individual *SS* bounce points, corrections must be applied for lateral velocity variations in the mantle. Current mantle tomography models (e.g. Masters & Bolton 1991; Woodward *et al.* 1992) apply corrections for differences in surface topography and crustal thickness before inverting the data for velocity structure. Thus, we must adjust the *SS–SdS* times for bounce-point topography and crustal thickness as well as apply corrections for deeper 3-D structure using the velocity models. Fig. 6(a) shows traveltime corrections to *SS* at 140° for topography and crustal thickness (using the method discussed in Woodward & Masters 1991). The *SS* arrivals are delayed on the continents relative to the ocean, due to the higher topography and thicker crust on the continents. The average global correction is −2.8 s and reflects the fact that oceans cover roughly 70 per cent of the surface. For *SS* − *SdS* at 140°, this 2.8 s correction will cause about an 8 km increase in the average apparent depth to the 410 km discontinuity, and an 11 km increase in the depth to the 660 km discontinuity.

In order to correct for mantle heterogeneity, two different shear velocity models are used and the results compared: model SH10C of Masters & Bolton (1991) and model SH8WM13 of Woodward *et al.* (1992). Lateral variations in each model are specified by spherical harmonics up to degree 10 for SH10C and degree 8 for SH8WM13. Model SH10C divides the mantle into 11 spherical shells of approximately equal thickness while SH8WM13 uses Chebyshev polynomials to specify a vertically smooth model. For each *SS–SdS* time, an iterative procedure is used to find the discontinuity depth at which the predicted *SS–SdS* time (corrected for perturbations along the *SS* ray between the surface and the discontinuity) is equal to the observed time (corrected for topography and crustal thickness). Perturbations along the *SS* and *SdS* rays below the discontinuity are ignored since they will be nearly identical for these low-order heterogeneity models.

These mantle heterogeneity models predict significant corrections to the apparent discontinuity depths obtained from *SS–SdS* times. Figs 6(b) and (c) show perturbations to

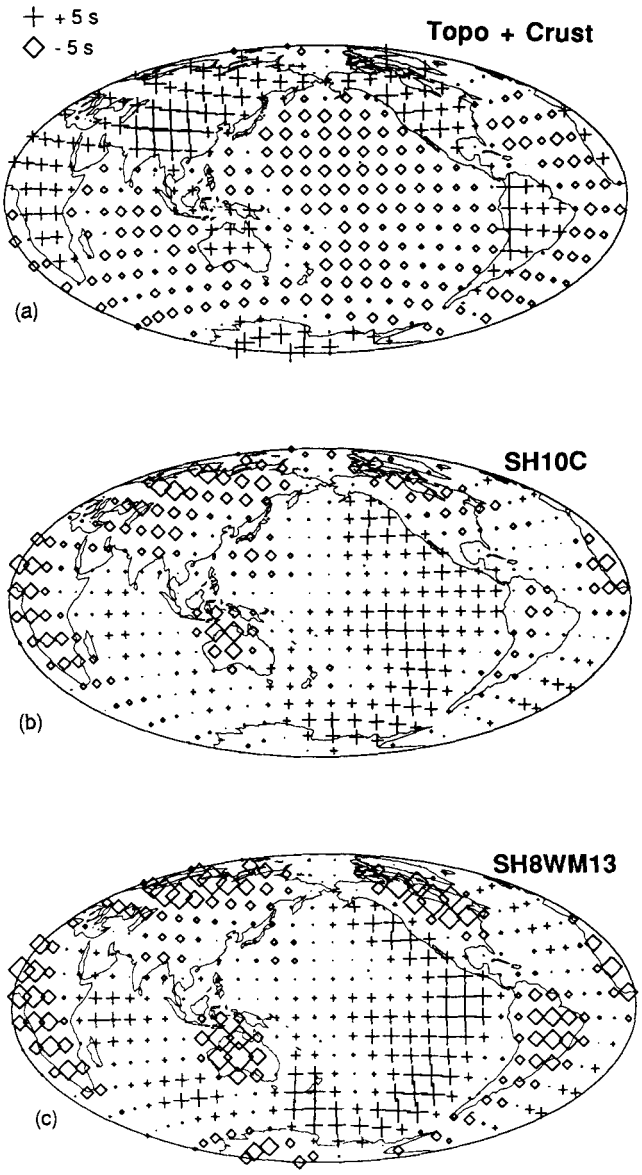

Figure 6. Perturbations to *SS* traveltimes at 140° (plotted at the bounce point). (a) Topography and crustal thickness differences. *SS* times are delayed on the continents due to their higher topography and thicker crust relative to the oceans. (b) Model SH10C structure between the surface and 660 km. (c) Model SH8WM13 structure between the surface and 660 km.

SS times at 140° resulting from structure between the surface and 660 km for the two models. Model SH10C predicts differences in *SS* traveltimes of −5 to 4 s, while SH8WM13 predicts anomalies of −7 to 6 s; each model has zero mean. These *SS* traveltime differences predict variations in the apparent depth to the 660 km discontinuity of 35 to 50 km. The corrections are comparable in size to the actual topography on the discontinuities (see below), so the accuracy of the corrections is very important. A comparison of Figs 6(b) and (c) shows that although SH10C and SH8WM13 agree quite well in the overall shape of the upper mantle heterogeneity pattern, there are significant differences between the models. The SH8WM13 anomalies are about 50 per cent larger than the SH10C anomalies and differ in some specific regions such as South America and Antarctica. Differences between SH10C and SH8WM13 are minimized in this plot which shows the integrated anomaly between the surface and 660 km; somewhat larger differences are seen between the models at shallower depths. These discrepancies will translate into differences in calculated topography on the major discontinuities, and uncertainties in the upper mantle velocity models are probably the largest source of error in the determination of discontinuity depths. In order to make these uncertainties clear, we present results obtained from separate analyses using each model.

A possible complication is the effect that the discontinuity perturbations have on the tomographic models, which are derived assuming no discontinuity topography. Fortunately, these effects are small since 410 and 660 km depth variations have much less influence on traveltimes for transmitted waves (used in the tomographic inversions) than for reflected waves (i.e. the *SS* precursors). Consider vertical wave propagation across a discontinuity with a shear velocity contrast of $\Delta\beta$ and a mean shear velocity of $\bar{\beta}$. A depth perturbation Δz will cause a traveltime change in the transmitted S wave of $\Delta t_{\text{trans}} = \Delta z \Delta\beta/\bar{\beta}^2$ (assuming $\Delta B \ll \bar{\beta}$) and a change in the reflected-wave traveltime (one-way) of $\Delta t_{\text{refl}} = \Delta z/\bar{\beta}$. The ratio of the transmitted-to-reflected traveltime changes is $\Delta t_{\text{trans}}/\Delta t_{\text{refl}} = \Delta\beta/\bar{\beta}$. For the PREM model near 660 km, $\Delta\beta/\bar{\beta} = 6.5$ per cent. Thus, a 15 km change in discontinuity depth will induce an anomaly in the tomographic models which will cause only a 1 km error in the corrections to the measured discontinuity depths. This is a second-order effect which we choose to ignore in this paper.

Our previous analyses of discontinuity depths from *SS* precursors (Shearer 1991; Shearer & Masters 1992) used *SS*–*S* times to correct for lateral velocity variations. This technique, while suitable for preliminary work, suffered from many limitations. The *SS*–*S* times provide only an approximation to the desired model of velocity variations in the upper mantle and have no depth resolution. They can be used to correct 660 km depths to the extent that the relatively weak mid-mantle heterogeneity (which will affect the *S* traveltime) can be ignored, but will give more biased results for 410 km depths since the effect of transition-zone heterogeneity will be incorrectly modelled. Finally, our prior analyses used raw *SS*–*S* times which we (erroneously) believed had not been corrected for bounce-point topography or crustal thickness. Since these bounce-point differences should then appear in the *SS*–*S* times, in principle by using these raw times we could directly correct for these differences. However, in fact the times we used had been adjusted for topography (but not for crustal thickness), so topographic corrections were not accounted for. This was a significant error since bounce-point topography predicts differences of several seconds in *SS* traveltimes between continents and oceans.

Our present analysis corrects these problems as well as using a more appropriate reference radial model for long-period data (PREM at 25 s). The inclusion of proper topographic corrections moves the discontinuities to deeper average depths (since the mean surface height is below sea-level), whereas the slower velocity model moves the discontinuities to shallower depths. Our current best

estimates of the mean discontinuity depths are 413 and 653 km, compared to our previous results of 415 and 659 km.

THE BINNING PROCEDURES

Although in principle discontinuity depths could be obtained at each of the *SS* bounce points shown in Fig. 4, in practice the apparent *SdS* arrival times are so scattered that stable depth estimates are derived only by averaging results from many seismograms. Shearer (1991) performed this averaging using a tectonic regionalization scheme and found no significant differences in average depths to the 410 and 660 km discontinuities between major tectonic regions, but found some evidence for a depression in the 660 km discontinuity near the subduction zones in the northwest Pacific. Shearer & Masters (1992) adopted a more direct approach of finding the average discontinuity depth within equally spaced caps of 10° radius and using these values to produce a global map of topography on the 660 km discontinuity. This map indicated depth variations in the 660 of up to 30 km, and confirmed the existence of a trough in the discontinuity behind the Kuril–Kamchatka subduction zone.

In this paper, we continue using the cap averaging scheme. Fig. 7 shows the centres of the 416 caps which are spaced approximately 10° apart. For each cap, histograms of discontinuity depths are produced for *SS* bounce points within a 10° radius (with some overlapping between adjacent caps). Fig. 8 shows each of the individual histograms of discontinuity depths from 0 to 1000 km. These are computed and smoothed in the same way as the histograms shown in Fig. 3, except the curves are self-scaled and only positive values are shown. The height of each curve is proportional to the fraction of seismograms which contain apparent *SdS* arrivals at a given depth. The cap number is shown to the left of each histogram; the locations of each cap can be found in Fig. 7. The number of seismograms within each cap is plotted to the right of histogram. 413 of the 416 caps contain at least one seismogram, while 338 caps contain 10 or more seismograms. Discontinuity depths have been corrected for topography, crustal thickness and mantle structure using model SH10C. The thin vertical lines are at 413 and 653 km, the globally averaged depths of the 410 and 660 km peaks.

The reliability of these histograms varies with the quantity of data that they are averaging. Caps containing a large number of seismograms generally have well-defined peaks for the 410, 520, and 660 km discontinuities. Caps 71 to 76, each containing over 200 traces, provide an example of this. The major discontinuities are generally not resolved for caps which contain 10 or fewer seismograms (e.g. caps 125 to 127). The largest peaks are usually found near 410 and 660 km, particularly for the caps with the most data. However, peaks at other depths are occasionally as high as or higher than the 410 and 660 km peaks. The triangles show the estimated depth (and standard error) of the 410 and 660 km discontinuities on individual histograms. These estimates are obtained by identifying the largest peak within 50 km of the target discontinuity depth in the smoothed histograms. In order to estimate standard errors for these discontinuity depths, a bootstrap method (e.g. Efron & Tibshirani 1991) is used which randomly resamples the data prior to the smoothing and peak identification. Discontinuity depths are only estimated for caps with 10 or more seismograms. The histograms are then checked by hand and depth estimates removed which appear unreliable due to low peak amplitudes or ambiguities from multiple peaks.

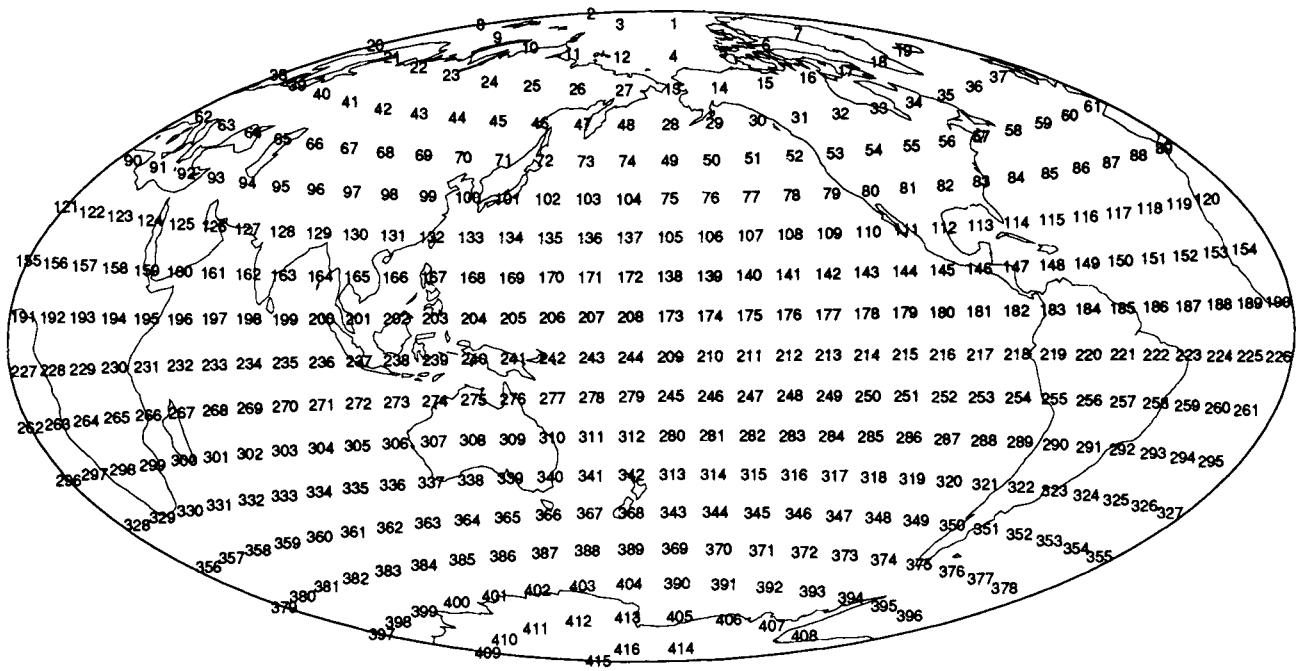

Figure 7. Locations of the 416 caps used to compute histograms of *SdS* arrivals (see Fig. 8). Caps are spaced approximately 10° apart.

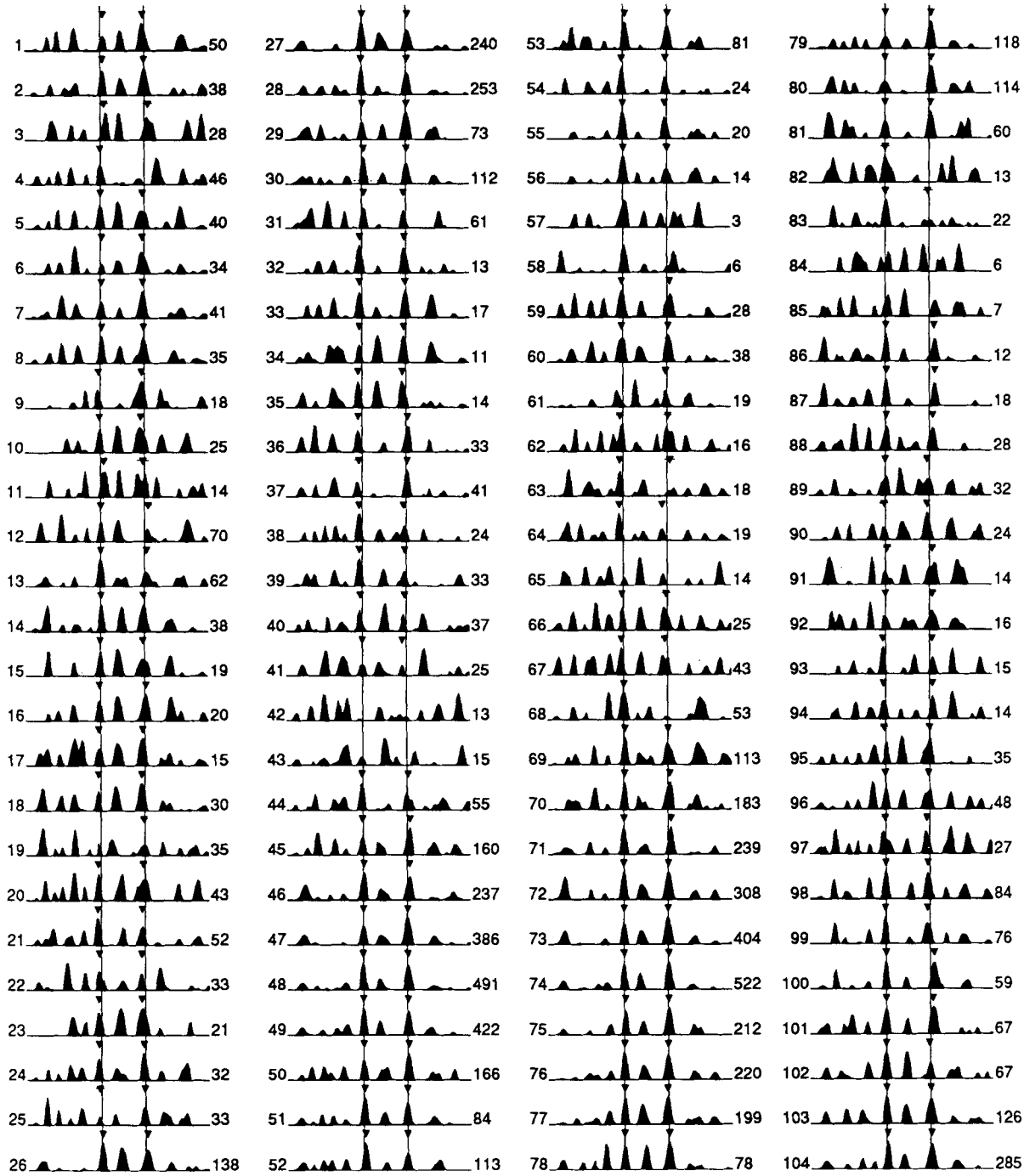

Figure 8. Histograms of apparent discontinuity depths from *SdS* arrivals observed in the cap locations shown in Fig. 7. Apparent depths have been corrected for bounce-point topography and crustal thickness, and for mantle velocity variations using SH10C. The cap number is shown to the left of each trace; the number of seismograms in the cap is labelled on the right. Histograms are smoothed with a $\cos^2$ function and self-scaled to uniform maximum amplitude with only positive values plotted. The vertical lines indicate depths of 413 and 653 km, the average apparent depths of the two major mantle discontinuities. The small triangles show the positions of the 410 and 660 km peaks as estimated by an automatic fitting procedure (see text). The horizontal lines bisecting these triangles indicate the standard errors associated with these estimates; in most cases these lines are too short to be visible.

Separate estimates of discontinuity depths are obtained for the raw data (no corrections for topography, crustal thickness or velocity models), the SH10C corrected times, and the SH8WM13 corrected times. A table of the discontinuity depth estimates and their standard errors at each of the cap locations is available from the author (E-mail address: pshearer@ucsd.edu).

MAPPING THE DISCONTINUITIES

Figures 9 and 10 map the apparent depths to the 410 and 660 km discontinuities at the cap locations. Depths are shown as residuals relative to the mean discontinuity depth for each map. Only depths with estimated standard errors less than 10 km are plotted. Results are shown for the raw

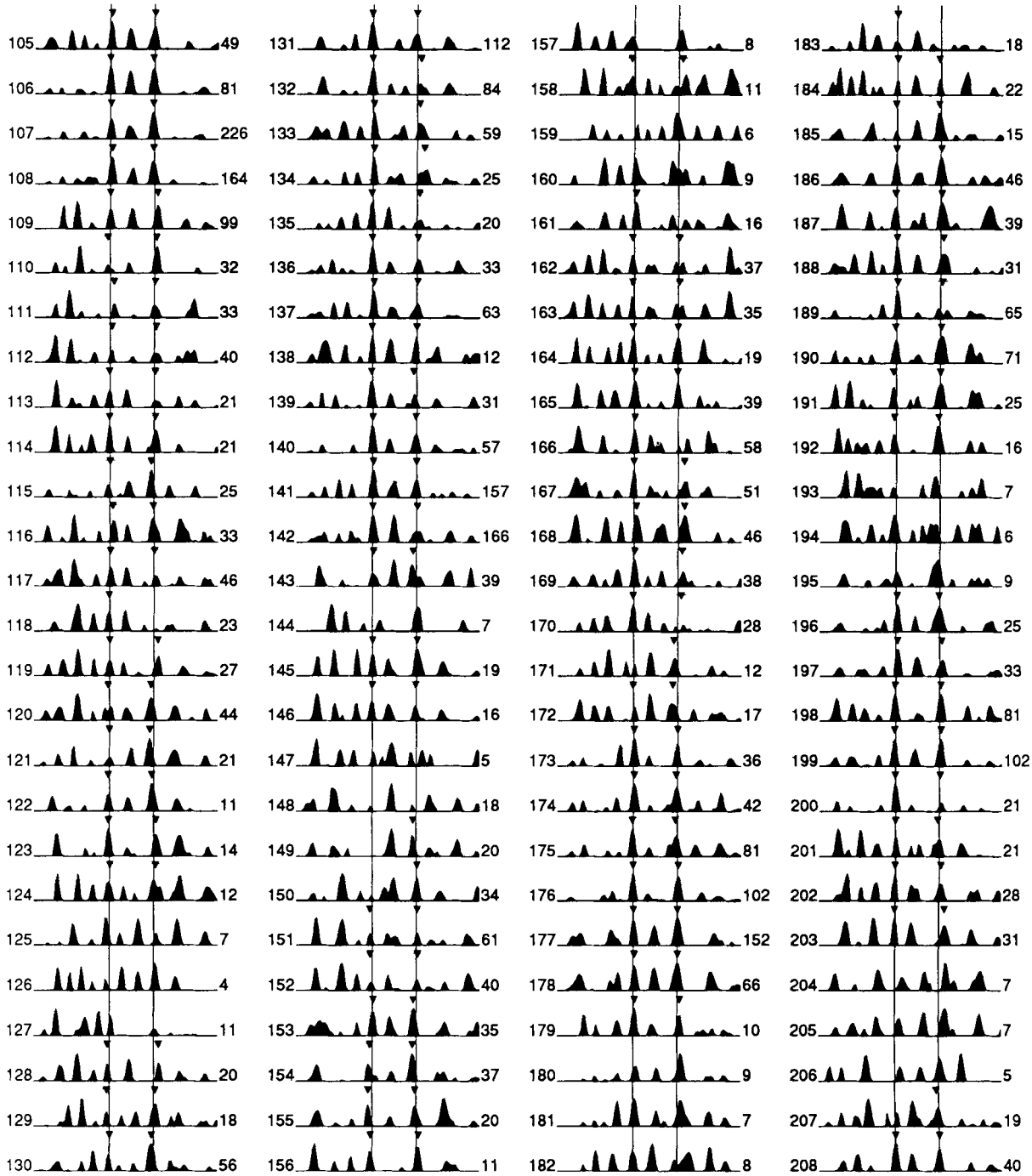

Figure 8. (*Continued.*)

SS–SdS times, the SH10C corrected times, and the SH8WM13 corrected times. The raw times include no topographic or crustal thickness corrections; the corrected times include these adjustments. The global average of discontinuity depths for the raw data (406 and 646 km) are less than the average depths for the corrected data (413 and 653 km) due to the non-zero mean of the topography and crustal corrections (see above). These maps indicate large-scale coherent patterns of discontinuity topography with up to about ±20 km of relief.

In order to produce smooth maps of discontinuity topography, we use the method of spherical splines on the cap-averaged depths and their standard errors. We require at least 10 seismograms per cap and standard errors in depth of less than 30 km. Results are shown in Fig. 11 for both discontinuities and models SH10C and SH8WM13. This technique gives the surface with the smallest second lateral derivative integrated over the sphere of a given target χ^2. We use a χ^2 of 300 for each fit; the number of data points varies from 311 to 327. Changing the target χ^2 so that the data are substantially over- or under-fitted results in maps of similar shape but with variable amplitude. The equivalent

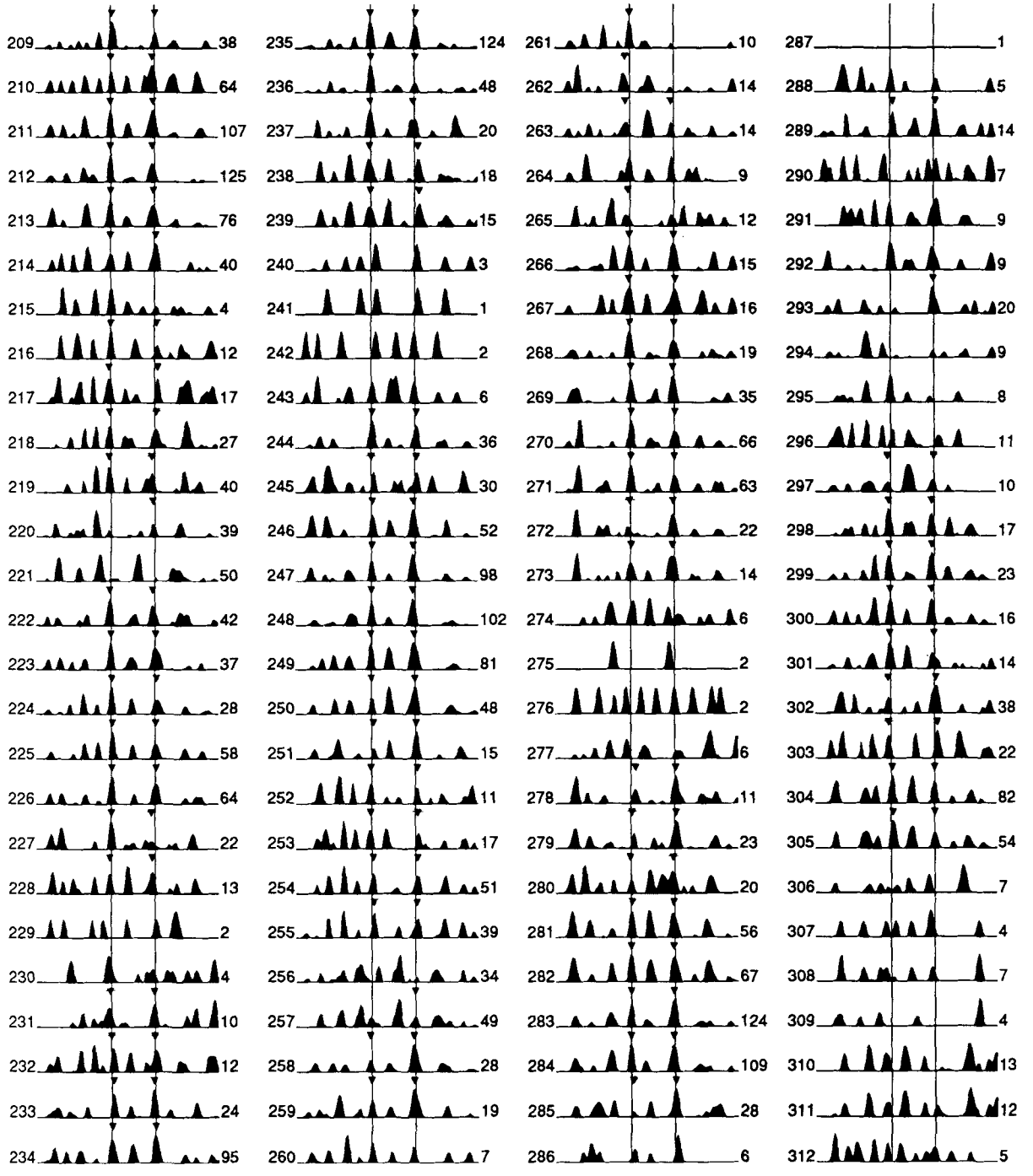

Figure 8. (*Continued.*)

spherical harmonic expansions for the surfaces shown in Fig. 11 are listed in Table 1 and have nearly all their power in the first eight harmonic degrees. Although the spherical spline method does not produce models with large structure in regions with no data, the topography shown in Fig. 11 should not be accepted without reference to Figs 9 and 10 to see where the data actually constrain the model. For example, the large depression shown in the 660 km discontinuity near the Phillipines results from a fairly small number of data points, and the structures near South America are largely interpolated from a sparse distribution of data.

Some differences are apparent between the SH10C and SH8WM13 corrected maps. The discontinuity highs in northern Canada and Eurasia are reduced for the SH8WM13 results, reflecting the higher upper mantle velocities in these regions for SH8WM13 compared with SH10C. Significant differences also exist for regions near South America, the Phillipines, Antarctica and New Zealand. The 660 km models also differ substantially from

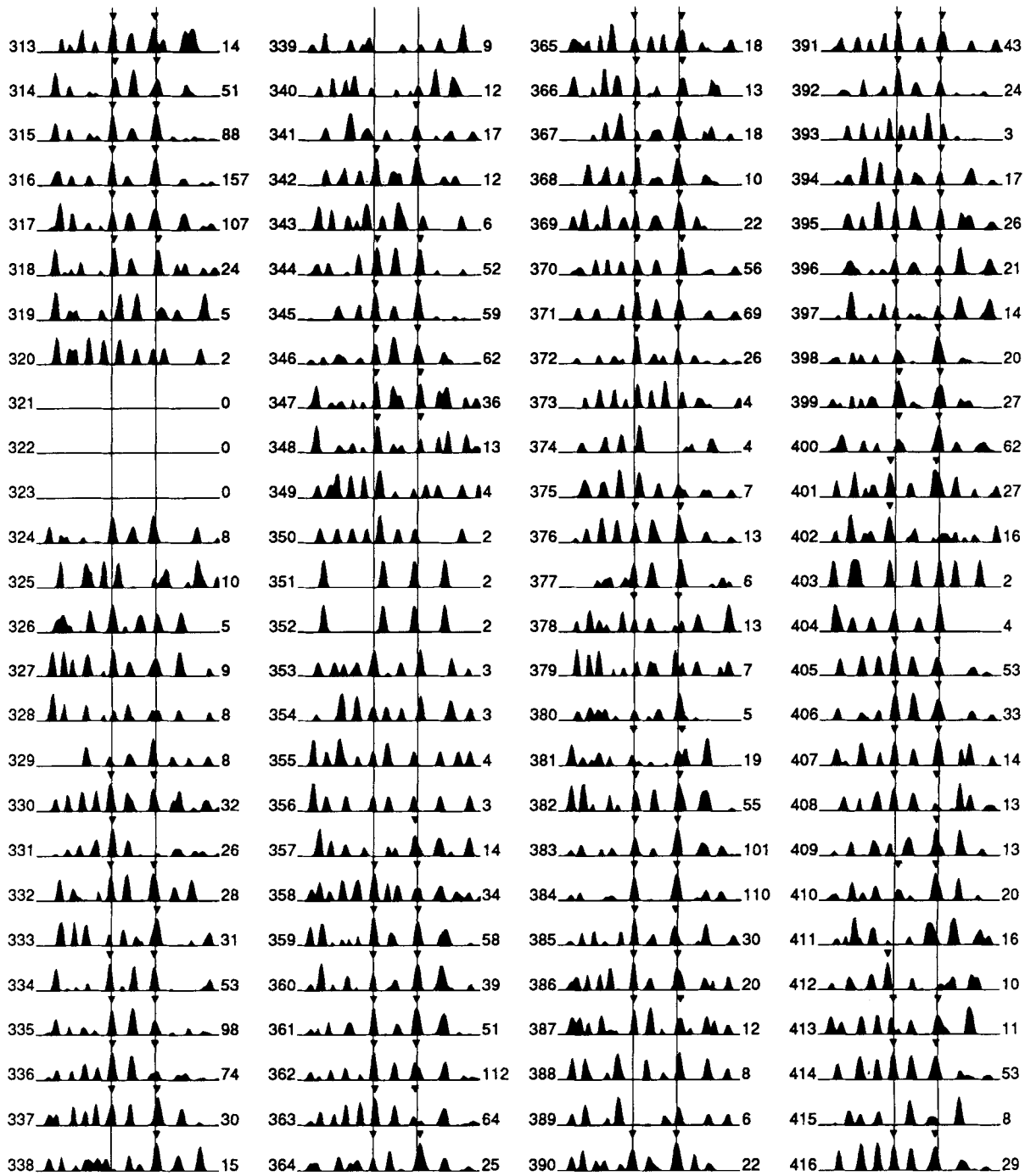

Figure 8. (*Continued.*)

model Topo660a (Shearer & Masters 1992). The newer models should be more accurate due to the increase in the number of seismograms used, the proper application of topographic corrections, and the use of velocity models rather than *SS–S* times to correct for mantle structure.

The apparent correlation between subduction zones and depressions in the 660 km discontinuity seen in model Topo660a is less convincing in the new models. The depression near Tonga is greatly reduced in size and the South American depression is suggested only in the SH8WM13 corrected model, although the sparse data coverage in both areas does not exclude the possibility of larger depressions. There is evidence for at least a localized depression in the 660 km discontinuity beneath the Tonga slab from studies of *S*-to-*P* conversions from deep-focus events (e.g. Bock & Ha 1984; Richards & Wicks 1990). The new models also show a significant depression in the 660 km discontinuity in the northeast Atlantic, a region not associated with current subduction. This feature is unlikely to be an artefact due to inadequate mantle corrections, since an analogous depression is not seen in the 410 km discontinuity (although this feature is not constrained by a

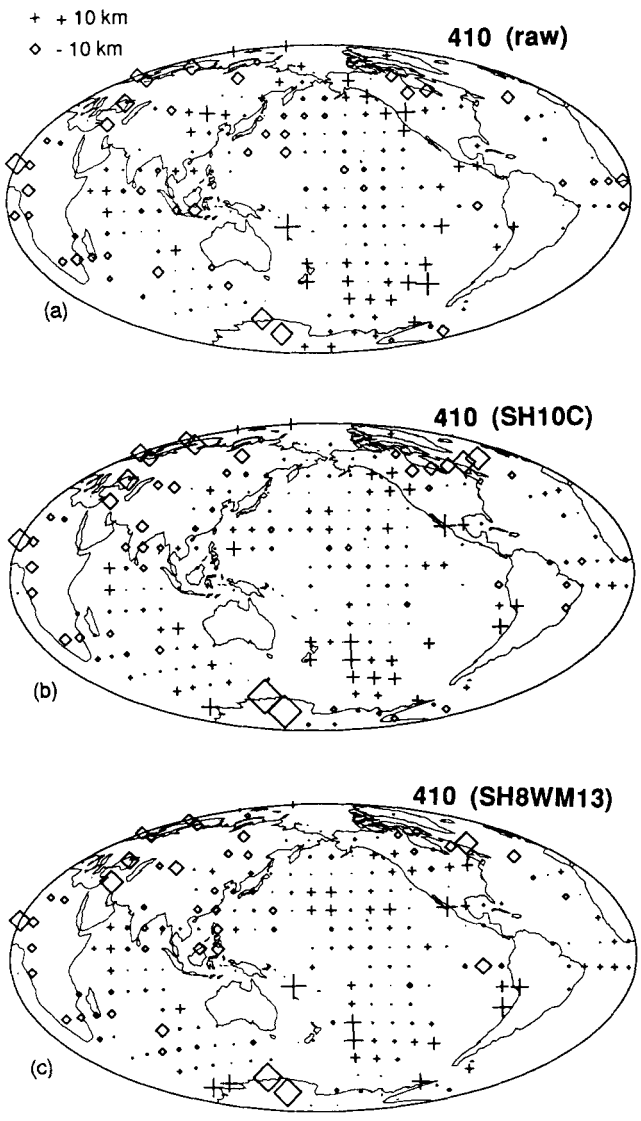

Figure 9. Depth anomalies to the 410 km discontinuity, plotted at the cap locations. Depths are plotted only if their estimated standard errors are less than 10 km and the caps contain 10 or more seismograms. (a) Raw depths, uncorrected for bounce-point topography, crustal thickness or mantle structure. Depths are relative to a mean discontinuity depth of 406 km. (b) Depths corrected for bounce-point topography, crustal thickness, and mantle model SH10C. (c) Depths corrected for bounce-point topography, crustal thickness and mantle model SH8WM13. The mean discontinuity depth for (b) and (c) is 413 km.

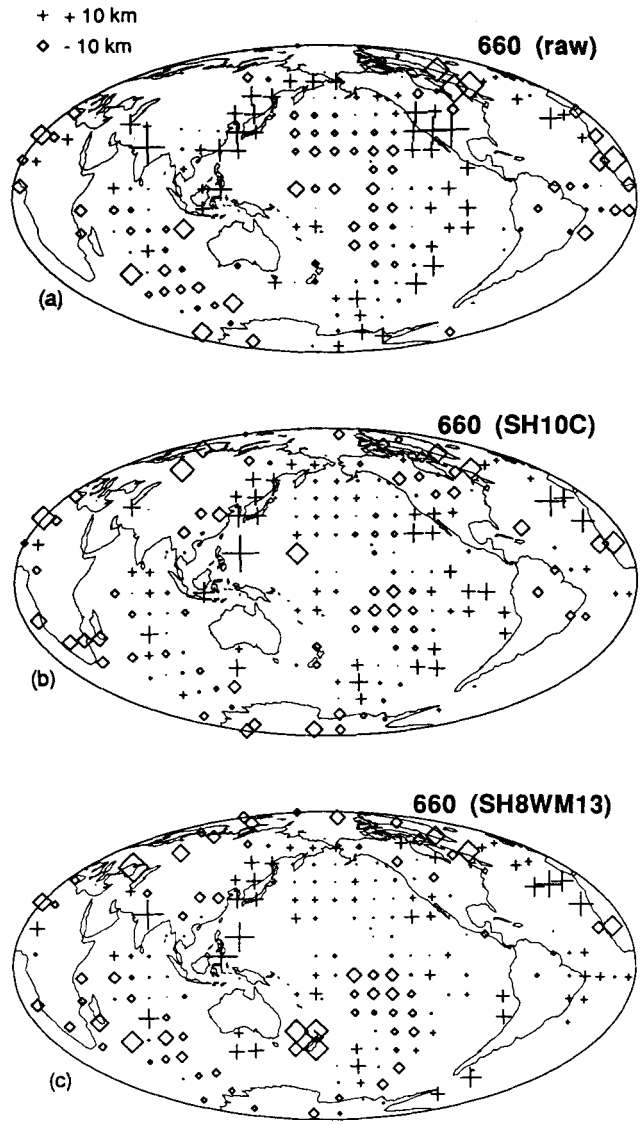

Figure 10. Maps of depth anomalies to the 660 km discontinuity, plotted at the cap location. Depths are plotted only if their estimated standard errors are less than 10 km and the caps contain 10 or more seismograms. (a) Raw depths, uncorrected for bounce-point topography, crustal thickness or mantle structure. Depths are relative to a mean discontinuity depth of 646 km. (b) Depths corrected for bounce-point topography, crustal thickness and mantle model SH10C. (c) Depths corrected for bounce-point topography, crustal thickness and mantle model SH8WM13. The mean discontinuity depth for (b) and (c) is 653 km.

large number of data). The most robust feature in the 660 km topography continues to be the depression in the northwest Pacific, which does not appear in the map of 410 km depths and is constrained by numerous *SS* bounce points.

As discussed in Shearer & Masters (1992), this trough appears associated with the Kuril–Kamchatka subduction zone and agrees roughly in position with recent topographic studies (van der Hilst *et al.* 1992; Fukao *et al.* 1992) which image fast horizontal velocity anomalies in the transition zone extending westward from the point at which the slabs intersect the 660 km discontinuity. Recent analyses of *S*-to-*P* conversions in this area indicate that this depression may be slightly deeper in the immediate vicinity of the slabs (Vidale & Benz 1992). In our new models this anomaly extends southward to the region around the Phillipines where it may be associated with the Phillipine and Mariana subduction zones. Unfortunately, the *SS* bounce-point distribution, while improved over that used in model Topo660a, is still too sparse to resolve the precise position of this southern anomaly relative to the subduction zones. However, it clearly is a significant feature, which, at least for the SH8WM13 corrected data, is associated with a slight elevation in the 410 km discontinuity. This is consistent with mineral physics predictions for a cold-temperature anomaly in the transition zone (see below).

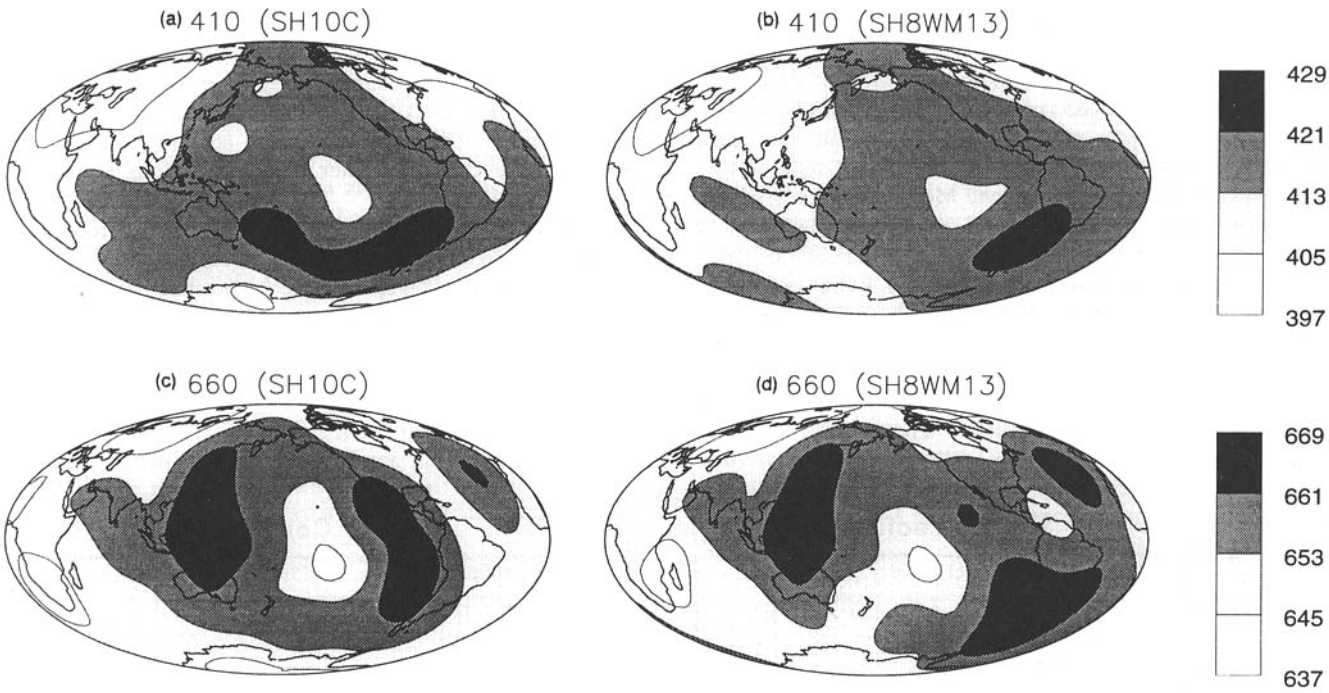

Figure 11. Smooth maps of topography on the 410 and 660 km discontinuities obtained using the method of spherical splines on the cap averages shown in Figs 9 and 10. Times are corrected for bounce-point topography and crustal thickness and for mantle velocity structure using either SH10C (a, c) or SH8WM13 (b, d). Spherical harmonic coefficients for these maps are listed in Table 1.

Table 1. Spherical harmonic coefficients for the spherical-spline models shown in Fig. 11. Coefficients are normalized as in Stacey (1977). Models 410b and 660b are SH10C corrected; 410c and 660c are SH8WM13 corrected.

Spherical Harmonic Coefficients for Model Topo410b

		$m=0$	1	2	3	4	5	6	7	8
C_0^m		413.169								
	S_0^m	0.000								
C_1^m		-2.184	-2.564							
	S_1^m	0.000	-1.718							
C_2^m		-0.810	-1.005	-0.589						
	S_2^m	0.000	-0.158	-0.821						
C_3^m		1.523	-1.421	0.367	-0.088					
	S_3^m	0.000	-0.831	-0.063	-0.076					
C_4^m		-0.571	-0.614	-0.362	0.860	0.353				
	S_4^m	0.000	0.681	0.359	-0.628	-0.655				
C_5^m		1.034	0.355	-0.094	0.120	-0.737	-0.064			
	S_5^m	0.000	0.105	-0.721	-0.224	-0.141	-0.457			
C_6^m		0.214	-0.090	-0.061	0.135	-0.032	-0.096	0.261		
	S_6^m	0.000	-0.006	0.531	-0.212	0.197	0.006	-0.252		
C_7^m		0.429	0.172	-0.044	0.137	0.037	-0.181	0.095	-0.068	
	S_7^m	0.000	-0.223	-0.163	-0.129	-0.040	0.085	0.016	-0.141	
C_8^m		0.200	0.012	0.031	0.137	-0.142	0.118	-0.020	-0.128	-0.084
	S_8^m	0.000	0.020	0.017	0.082	-0.146	0.027	-0.041	0.124	0.015

Spherical Harmonic Coefficients for Model Topo410c

		$m=0$	1	2	3	4	5	6	7	8
C_0^m		413.030								
	S_0^m	0.000								
C_1^m		-1.511	-1.376							
	S_1^m	0.000	-2.608							
C_2^m		-0.408	-1.696	-0.224						
	S_2^m	0.000	0.161	-0.698						
C_3^m		0.885	-0.701	-0.092	-0.903					
	S_3^m	0.000	-0.475	0.629	-0.700					
C_4^m		-0.180	-0.256	-0.421	0.376	0.578				
	S_4^m	0.000	0.765	0.282	-0.048	-0.428				
C_5^m		0.492	0.575	-0.068	0.160	-0.132	-0.037			
	S_5^m	0.000	0.454	-0.553	0.130	-0.379	-0.139			
C_6^m		0.322	-0.063	-0.001	0.118	0.182	0.009	0.175		
	S_6^m	0.000	-0.045	0.314	-0.016	0.276	0.148	-0.235		
C_7^m		0.280	0.042	-0.045	0.122	0.167	-0.101	0.131	-0.096	
	S_7^m	0.000	-0.122	0.057	0.046	-0.064	-0.039	-0.051	-0.123	
C_8^m		0.094	-0.049	0.006	0.224	-0.150	0.139	-0.042	-0.103	-0.055
	S_8^m	0.000	0.025	0.093	0.060	-0.071	0.083	-0.017	0.109	0.047

Table 1. (*continued.*)

Spherical Harmonic Coefficients for Model Topo660b

		$m=0$	1	2	3	4	5	6	7	8
C_0^m		653.510								
	S_0^m	0.000								
C_1^m		0.162	-3.081							
	S_1^m	0.000	-0.352							
C_2^m		-1.769	-0.234	-2.093						
	S_2^m	0.000	0.631	-2.226						
C_3^m		-0.596	-0.682	0.915	0.977					
	S_3^m	0.000	-0.863	-0.171	1.418					
C_4^m		-0.881	-0.389	0.549	0.702	-0.441				
	S_4^m	0.000	0.197	-0.280	-0.693	-1.569				
C_5^m		0.782	-0.566	0.266	-0.026	-1.148	-0.423			
	S_5^m	0.000	0.224	-0.899	-0.494	-0.460	-0.470			
C_6^m		-0.360	-0.280	0.463	0.330	-0.486	-0.371	-0.022		
	S_6^m	0.000	0.076	-0.112	-0.053	0.016	0.133	0.396		
C_7^m		0.223	0.065	-0.076	0.135	0.323	-0.126	0.007	-0.448	
	S_7^m	0.000	-0.131	-0.003	-0.273	-0.113	-0.427	0.190	-0.055	
C_8^m		0.056	-0.012	-0.026	0.144	0.052	-0.203	0.160	-0.321	0.168
	S_8^m	0.000	-0.112	-0.019	-0.036	0.267	-0.089	0.135	0.070	-0.036

Spherical Harmonic Coefficients for Model Topo660c

		$m=0$	1	2	3	4	5	6	7	8
C_0^m		654.159								
	S_0^m	0.000								
C_1^m		-0.228	-1.152							
	S_1^m	0.000	-1.400							
C_2^m		-1.411	-1.571	-1.187						
	S_2^m	0.000	1.522	-3.550						
C_3^m		-1.024	0.041	0.659	1.118					
	S_3^m	0.000	-1.318	0.445	0.229					
C_4^m		-0.936	-0.418	0.347	0.236	-0.819				
	S_4^m	0.000	0.007	-0.985	-0.414	-0.884				
C_5^m		0.281	-0.708	-0.059	-0.259	-0.825	-0.202			
	S_5^m	0.000	0.329	-0.946	-0.639	-0.616	-0.263			
C_6^m		-0.169	-0.252	0.362	0.277	-0.362	-0.100	-0.028		
	S_6^m	0.000	0.219	-0.123	0.169	0.223	0.104	0.606		
C_7^m		0.194	0.035	-0.160	0.312	0.392	0.084	-0.126	-0.583	
	S_7^m	0.000	0.000	0.308	-0.090	-0.398	-0.657	0.206	0.068	
C_8^m		-0.073	-0.076	-0.029	0.321	-0.023	-0.180	0.038	-0.234	0.105
	S_8^m	0.000	-0.140	0.114	0.133	0.329	-0.009	0.259	0.114	0.055

410 VERSUS 660 DEPTHS

Since mineral physics data indicate that the Clapeyron slopes of the 410 and 660 km phase changes are of opposite signs, depths to these discontinuities should be anti-correlated, assuming vertically coherent temperature anomalies in the transition zone. Measured values of the Clapeyron slope for the olivine→β-phase change near 410 km include $\gamma = 2.5$ MPa/°K (Ashida, Kume & Ito 1987), $\gamma = 2.5$ MPa/°K (Katsura & Ito 1989), and $\gamma = 1.5 \pm 0.8$ MPa/°K (Akaogi, Ito & Navrotsky 1989). These positive values of γ_{410} indicate an exothermic reaction in which the discontinuity moves toward deeper depths at higher temperatures. Values obtained for the γ-spinel→perovskite + magnesiowüstite phase change near 660 km include $\gamma = -2.0$ MPa/°K (Ito & Yamada 1982), $\gamma = -2.8$ MPa/°K (Ito & Takahashi 1989), and $\gamma = -4.0 \pm 2.0$ MPa/°K (Ito *et al.* 1990). The negative Clapeyron slopes for the 660 km phase change imply an endothermic reaction in which the discontinuity moves upward at higher temperatures. Thus, the 410 and 660 km discontinuities should move closer together in warm regions and further apart in cold regions.

Revenaugh & Jordan (1991a) find evidence for such a negative correlation from *ScS* reverberation data, while Stammler *et al.* (1992) observe a positive correlation in *P*-to-*SV* conversions which they attribute to the effect of lateral heterogeneity above the transition zone. Corrections for lateral heterogeneity are critical for these comparisons since either under- or over-correcting the data for heterogeneity above 400 km can introduce spurious correlations between 410 and 660 km depths. Fig. 12 plots

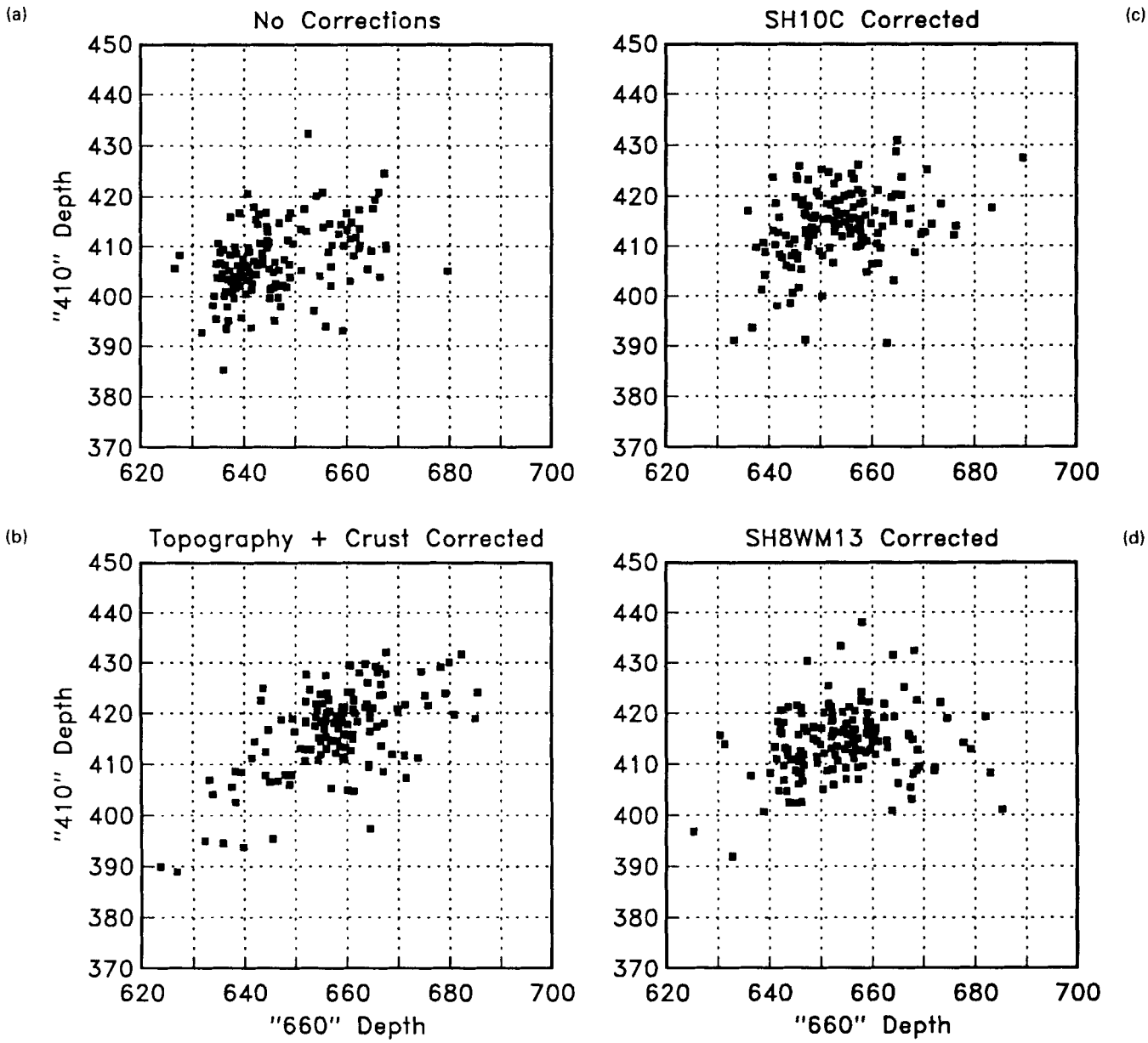

Figure 12. 410 versus 660 km discontinuity depths for (a) raw *SdS* times, (b) topography and crustal-thickness corrected times, (c) SH10C corrected times, (d) SH8WM13 times. Points are plotted only if both estimated standard errors are less than 10 km and the averaging cap contains 10 or more seismograms.

410 versus 660 depths for the cap-averaged values plotted in Figs 9 and 10. Results are shown for the raw *SS–SdS* times, the topography and crustal-thickness corrected times, and the SH10C and SH8WM13 corrected times. All of these plots suggest a weak positive correlation between the discontinuity depths. The corrections for topography and crustal thickness, when applied alone, actually increase the spread in the apparent depths. The variance in the depths is then reduced somewhat when the SH10C and SH8WM13 corrections are applied. This is consistent with the observed negative correlation between the topography and crustal corrections and the shallow velocity structure in mantle models (e.g. Woodward & Masters 1992). The SH8WM13 corrected values show the weakest positive correlation of any of the plots. If the two shallow depth points to the lower left (from caps near the Black Sea and Newfoundland) were removed, this plot would show little or no correlation.

It is likely that the positive correlations shown in Fig. 12 result from inadequate corrections for the velocity structure above 400 km, but it is difficult to quantify this argument. To the extent that one believes that the depths should be anti-correlated, the SH8WM13 corrections appear to come somewhat closer to producing the desired result. In all cases, the depths to the 660 km discontinuity exhibit greater variability than depths to the 410 km discontinuity. The greater variability in the 660 km depths is also seen in other discontinuity phases (Shearer 1991), and is consistent with the most recent laboratory measurements which indicate that the Clapeyron slope of the 660 km phase change is significantly larger in magnitude than the slope for the 410 km discontinuity.

A different test of the sign of the Clapeyron slopes of the 410 and 660 km discontinuities can be made by comparing discontinuity depths with SH10C and SH8WM13 velocity anomalies. Fig. 13 compares apparent discontinuity depths with the average *SS* traveltime anomaly across the transition

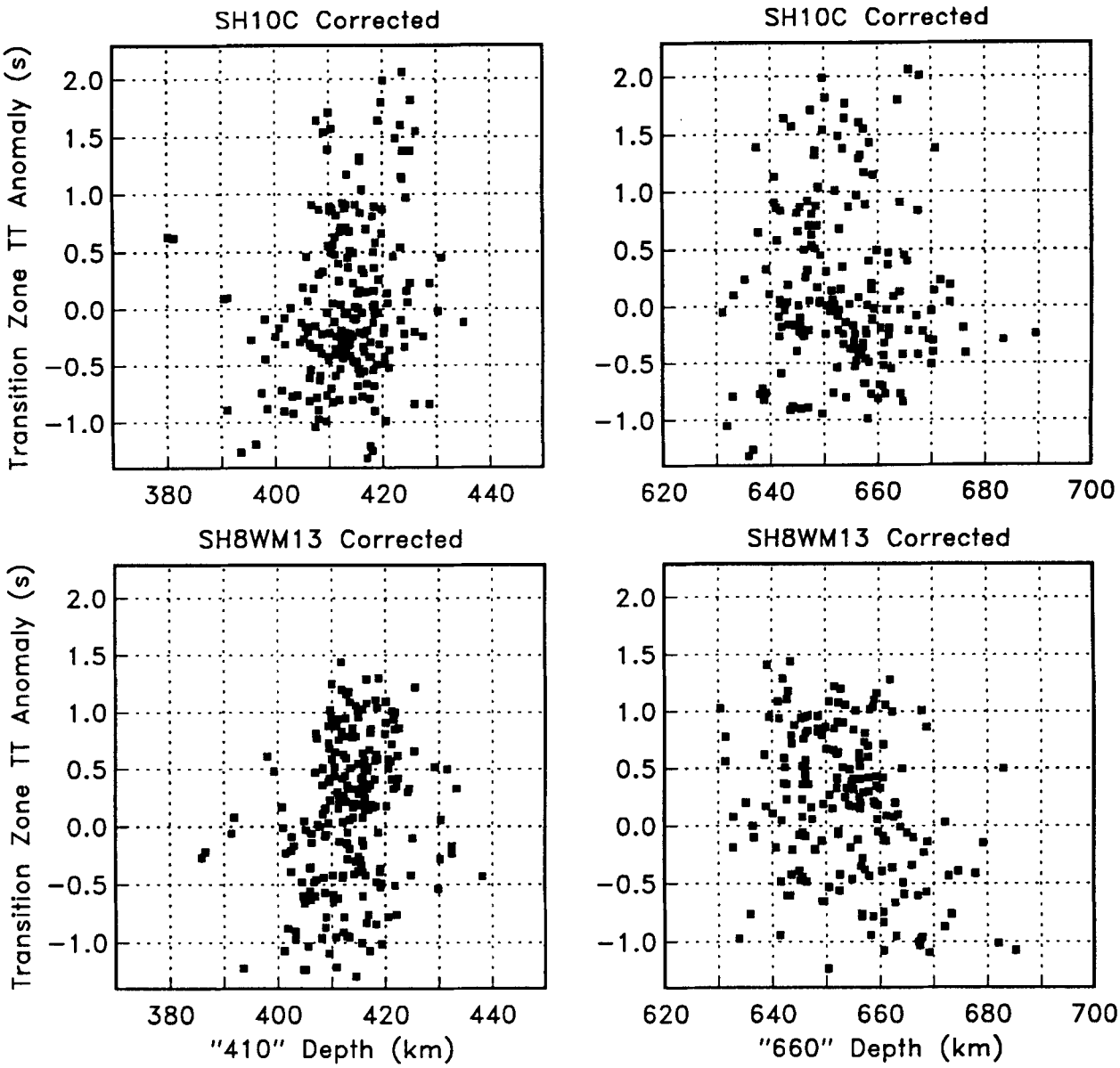

Figure 13. 410 and 660 km discontinuity depths versus transition-zone *SS* traveltime anomalies for mantle velocity models SH10C and SH8WM13. Traveltime anomalies are computed for individual ray paths and then averaged in the appropriate caps. Depths have been corrected for the appropriate model in each case.

zone for rays within the same cap. Negative traveltime anomalies indicate faster velocities and presumably colder temperatures. Colder temperatures should elevate the 410 km discontinuity and depress the 660 km discontinuity; thus we should expect to see a positive correlation between transition-zone traveltime anomalies and discontinuity depths for the 410 km discontinuity, and a negative correlation for the 660 km discontinuity. Although the data exhibit considerable scatter, they appear roughly consistent with this picture.

The transition-zone thickness as measured by the differential depth $d_{660} - d_{410}$ should be relatively unaffected by lateral heterogeneity above 400 km, and maps of this thickness probably provide a less biased measure of discontinuity structure than either of the individual maps of discontinuity depths. Fig. 14 shows a map of d_{660}–d_{410} for those caps with an estimated standard error in depth of 15 km or less. The small differences between these maps are due to variations in the transition-zone velocities in models SH10C and SH8WM13. A region of increased transition-zone thickness is seen in the northwest Pacific, consistent with the trough in the 660 km discontinuity in this region. This confirms that this feature cannot be a result of inadequate corrections for lateral heterogeneity above 400 km. The existence of a depression in the 660 km discontinuity in the northeastern Atlantic is also supported by an apparent increase in transition-zone thickness. In contrast, the depression seen in the '660' in southwestern North America appears to be less reliable since it is not clear in the transition-zone thickness map.

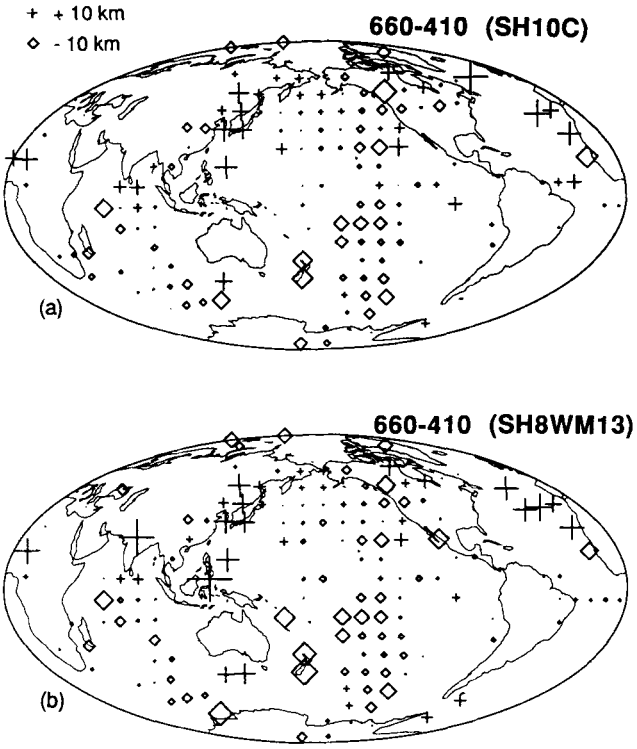

Figure 14. Maps of thickness anomalies for the transition zone, defined as d_{660}–d_{410} for (a) SH10C-corrected times, and (b) SH8WM13-corrected times. Points are plotted only if their estimated standard errors are less than 15 km and the caps contain 10 or more seismograms. Thicknesses are relative to the mean transition-zone thickness of 240 km.

Taken at face value, the overall pattern in Fig. 14 indicates cold transition-zone temperatures in the western Pacific and northeastern Atlantic, and warm temperatures in the southern Pacific and Indian Oceans. Since these temperature anomalies should also cause variations in seismic velocities, we might expect to see a correlation between apparent transition-zone thickness and traveltime anomalies within the transition zone. Fig. 15 shows *SS* traveltime anomalies from SH10C and SH8WM13 for structure between 410 and 660 km, compared with transition-zone thickness. Since the computed transition-zone thickness depends slightly upon the transition-zone velocity anomalies (which could produce a spurious correlation), results are shown both before and after correcting the discontinuity depths for these anomalies. As predicted, a negative correlation can be seen between the traveltime anomalies and d_{660}–d_{410} for the depth-corrected plots. The SH8WM13 velocity anomalies show the clearest negative correlation, even with the uncorrected depths.

These results show that depths to the 410 and 660 km discontinuities appear to be roughly correlated with mantle anomalies in the sense that is predicted by laboratory measurements of Clapeyron slopes for the appropriate phase changes. Eventually it may be possible to use these results to help calibrate the relationship between temperature and velocity perturbations in the transition zone. A good target area for such a study is the northwest Pacific, where a large well-resolved depression in the 660 km discontinuity appears to correlate with a fast velocity anomaly in the transition zone (e.g. Masters *et al.* 1982; Woodhouse & Dziewonski 1984; Fukao *et al.* 1992).

AMPLITUDE ANALYSIS

The cross-correlation method used to obtain *SdS* arrival times also provides a measure of the apparent amplitude of the *SdS* pulse relative to *SS*. These amplitudes tend to be biased toward large values, making the absolute amplitude information difficult to interpret (see discussion in Shearer 1919), but relative amplitude comparisons are still of interest. Fig. 16 maps average amplitude anomalies for $S_{410}S$ and $S_{660}S$ arrivals at the cap locations. The amplitudes are determined by computing the average amplitude of *SdS* phases for discontinuity depths within 30 km of the peaks in the depth histograms. The amplitudes exhibit some spatial coherence, but these patterns do not appear to correlate with the depth anomalies plotted in Figs 9 and 10. This is confirmed by the scatter in Figs 17(a) and (b) which plot 410 and 660 amplitudes versus discontinuity depths, and indicate no clear correlation between amplitude and depth. In contrast, Revenaugh & Jordan (1991a), using *ScS* reverberation data, observed a correlation between the *S*-wave reflection coefficient and apparent depth to the 660 km discontinuity, with the reflection coefficient becoming smaller as the discontinuity becomes deeper. Their results indicated about a factor of 2 change in the reflection coefficient for a 30 km change in depth. The results shown in Fig. 17 are inconsistent with such a strong dependence of the reflection coefficient with discontinuity depth on a global scale. However, it is still possible that such a dependence may occur in specific regions such as those in the Revenaugh & Jordan study.

What is the cause of the large amplitude variations seen in

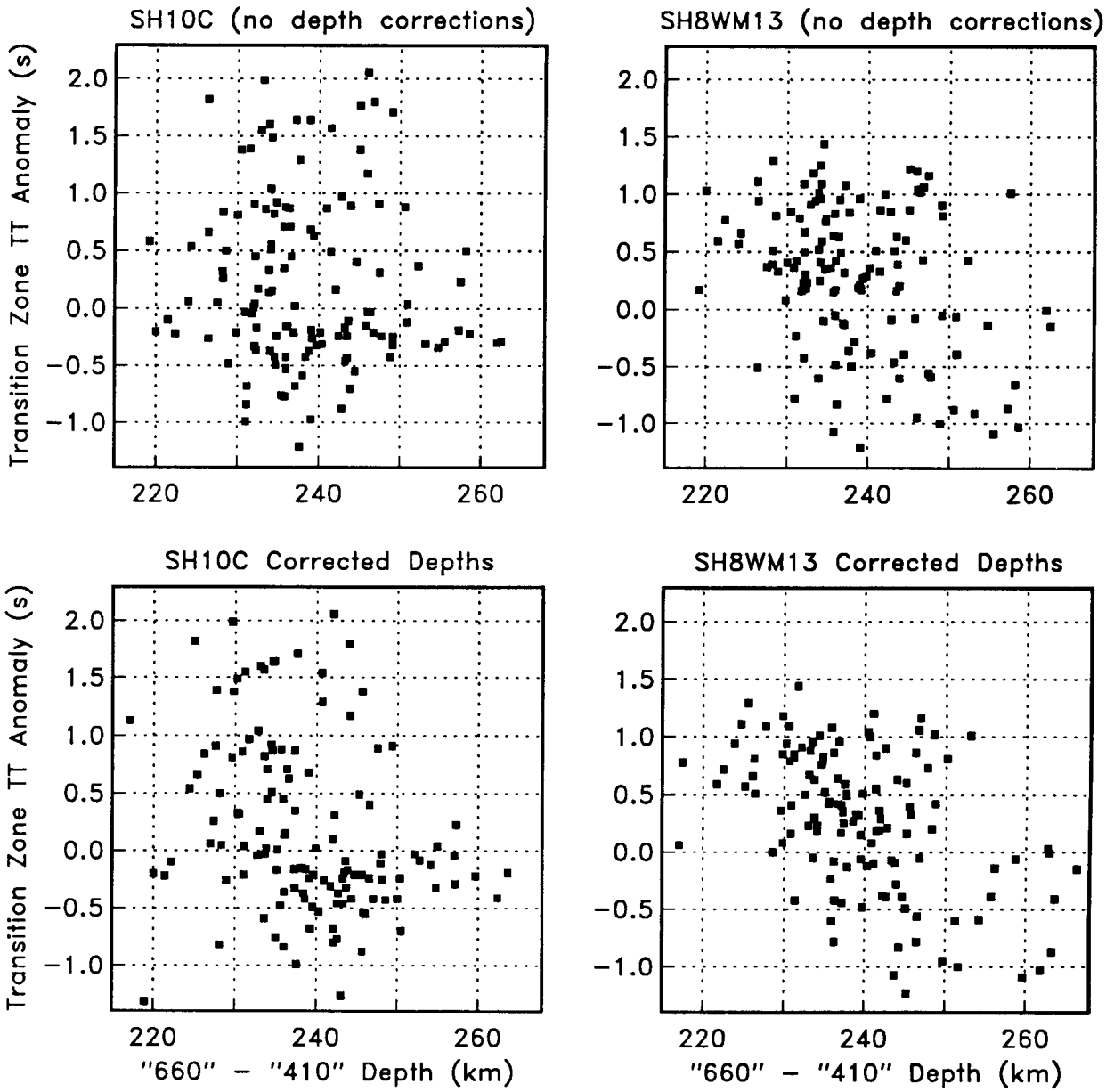

Figure 15. Transition-zone *SS* traveltime anomalies versus transition-zone thickness anomalies for mantle velocity models SH10C and SH8WM13. Traveltime anomalies are computed for individual ray paths and then averaged in the appropriate caps. Points are plotted only if their estimated standard errors are less than 15 km and the caps contain 10 or more seismograms. In the bottom plots the thicknesses are computed from depths corrected for the appropriate model. The negative correlation seen in the lower plots is consistent with vertically coherent temperature anomalies in the transition zone and laboratory results which indicate opposite signs for the Clapeyron slopes of the 410 and 660 km phase changes.

the *SdS* arrivals? Although $S_{410}S$ and $S_{660}S$ amplitudes do not appear correlated with discontinuity depth, they are strongly correlated with each other (see Fig. 17c). This argues against the amplitude variations being a result of focusing or defocusing effects caused by discontinuity topography, since it is probable that the depths to the discontinuities are anti-correlated (see above). (It is interesting to note that *SdS* rays are focused not by simple hills or valleys in the discontinuities, but rather by saddle-shaped structures, see discussion below). It is more likely that the amplitude variability is a result of focusing or defocusing along the *SdS* and *SS* ray paths due to velocity heterogeneity. In this case differences in the $S_{410}S$ and $S_{660}S$ amplitudes are not directly related to any properties of the discontinuities themselves.

REFLECTORS ABOVE 410 KM?

In addition to the major discontinuities near 410 and 660 km in the upper mantle, there have been numerous observations of additional reflectors at other depths (Fig. 1). The *P*-wave refraction analyses of Dey-Sarkar & Wiggins (1976) in western Canada, and Hales, Muirhead & Rynn (1980) in northern Australia, are particularly notable for the

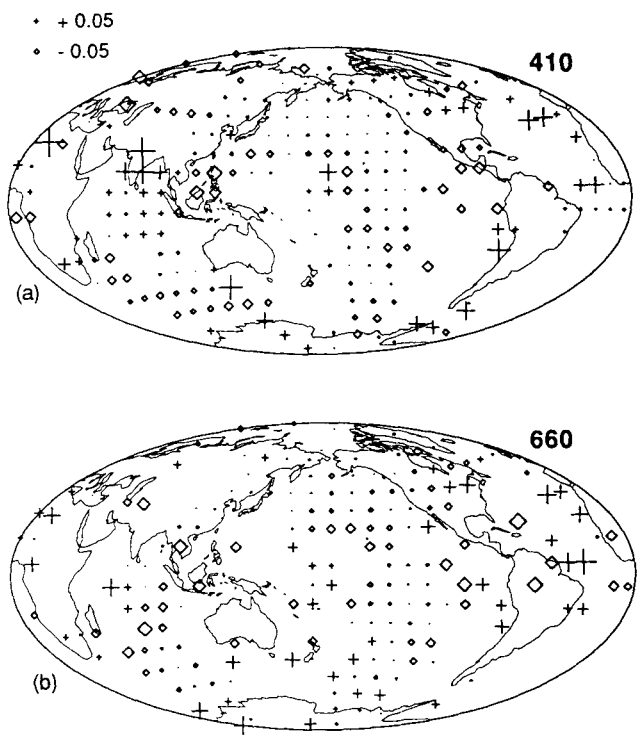

Figure 16. Maps of average amplitude anomalies for the $S_{410}S$ and $S_{660}S$ phases. Points are plotted only if the estimated standard error in depth is less than 10 km and the averaging cap contains 10 or more seismograms. Amplitudes are shown relative to the mean $S_{410}S/SS$-amplitude ratio of 0.29 and the $S_{660}S/SS$-amplitude ratio of 0.27.

number of upper mantle discontinuities for which they found evidence. However, many other analyses have produced much smoother models with discontinuities only near 410 and 660 km. Owing to differences in modelling assumptions it is difficult to judge the significance of the presence or absence of a discontinuity in a particular model.

Using *ScS*-reverberation data, Revenaugh & Jordan (1991a,b) found reflectors near 520, 710 and 980 km and at a variety of depths above 400 km. Revenaugh & Jordan (1991a) grouped the latter features into what they termed the *H* discontinuity (43 to 89 km), the *G* discontinuity (51 to 93 km, negative velocity contrast), the *L* discontinuity (186 to 281 km), and the *X* discontinuity (278 to 343 km). Recent global stacks of long-period body wave data have highlighted the existence of discontinuities near 410, 520 and 660 km, but find no clear evidence for discontinuities above 400 km (Shearer 1990, 1991). However, regional reflectors might not show up in these stacks, particularly if they are highly variable in depth as the Revenaugh & Jordan results suggest. The individual histograms shown in Fig. 8 contain numerous peaks in addition to those at 410, 520 and 660 km. In some cases these features appear to be coherent between adjacent cells. For example, a peak near 130 km appears in

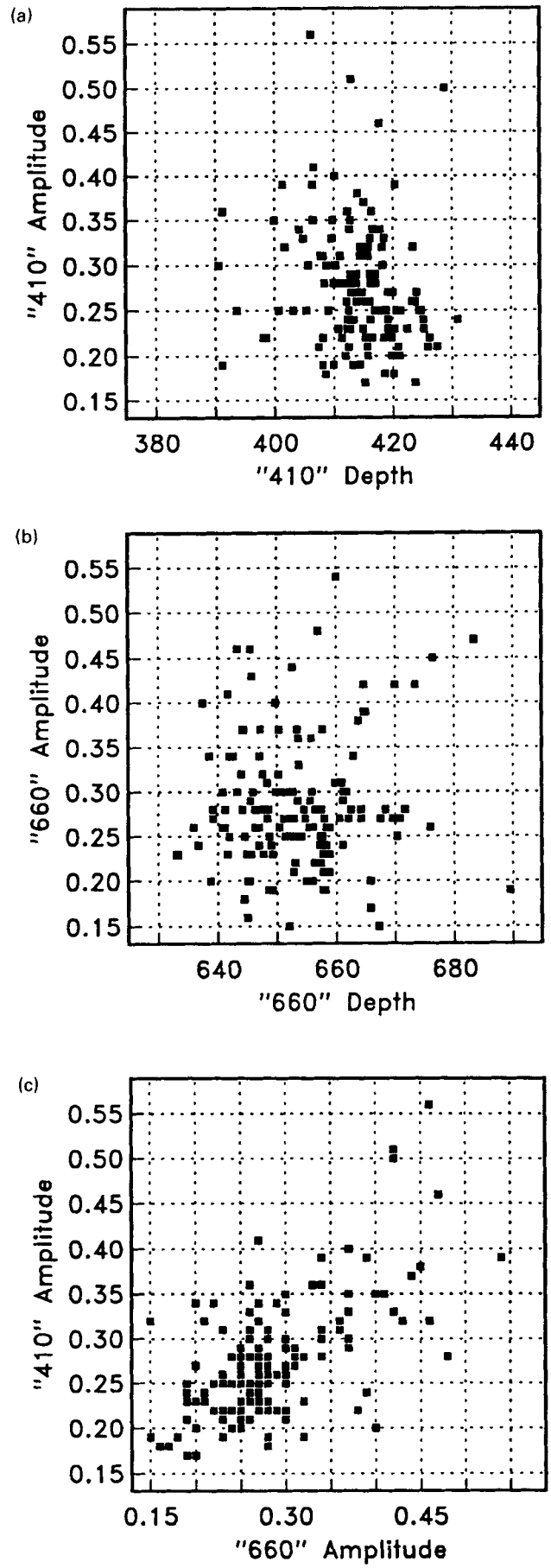

Figure 17. Plots of amplitudes and depths for the 410 and 660 km discontinuities. (a) Amplitude versus depth for the 410 km discontinuity. (b) Amplitude versus depth for the 660 km discontinuity. (c) $S_{410}S$ versus $S_{660}S$ amplitudes. Points are plotted only if the estimated standard error in depth is less than 10 km and the averaging cap contains 10 or more seismograms.

caps 269 to 273 in the Indian Ocean. These features do not occur at uniform depths over the globe, which is why no consistent peaks appear in the histograms shown in Fig. 3.

It is difficult to visualize the geographic distribution of the peaks in Fig. 8 and the degree to which they are spatially coherent. An alternative way of presenting these histograms is shown in Fig. 18 which displays slices at 20 km depth intervals throughout the upper mantle. The value of each histogram at a particular depth is shown at the cap location with black circles for positive correlations and open circles for negative correlations. The size of each circle is proportional to the fraction of seismograms containing a pick near the appropriate depth (actually the difference between the positively correlated picks and the negatively correlated picks). The histogram values are not self-scaled as in Fig. 8; a circle diameter of ~10° corresponds to picks

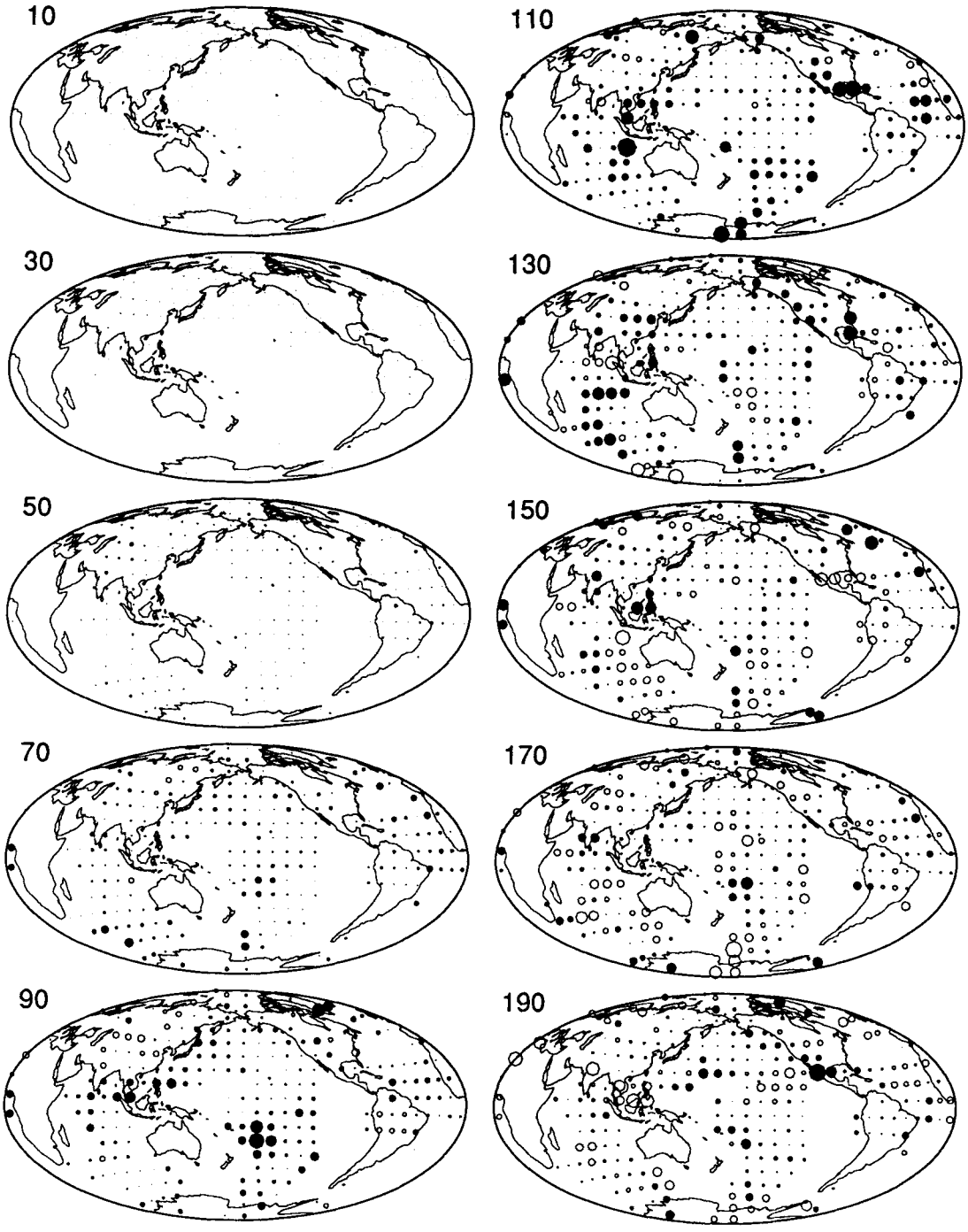

Figure 18. Apparent discontinuity depth histograms shown as slices at 20 km depth increments from 20 to 1000 km. The histograms are computed and smoothed the same as those shown in Fig. 8 except that they are not self-scaled. Positive values are shown as solid circles, negative values as open circles. Caps are shown only if they contain 20 or more seismograms. A circle of 10° radius indicates 25 per cent of the seismograms contain picks at that depth.

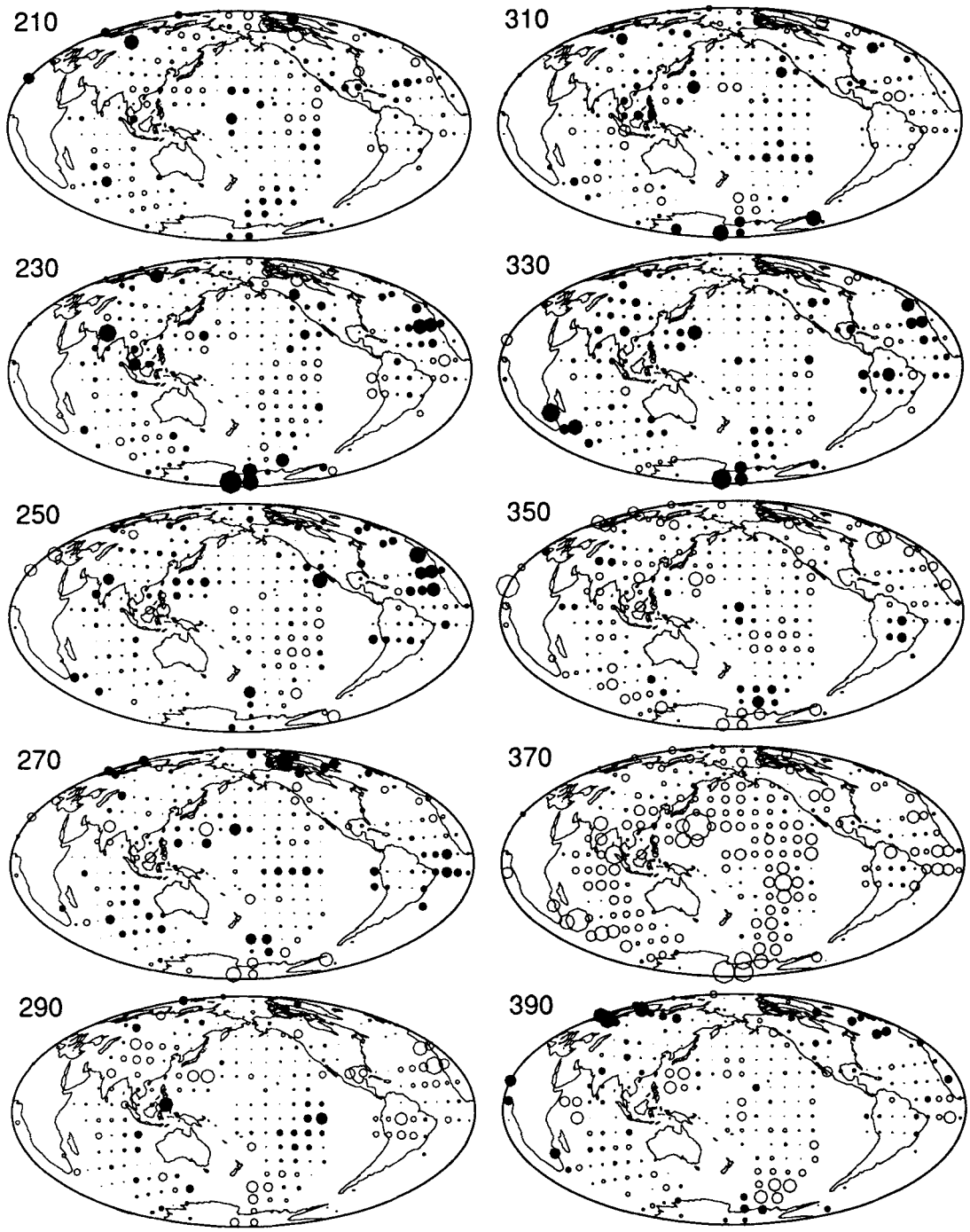

Figure 18. (*Continued.*)

on 25 per cent of the seismograms. Caps are plotted only if they contain 20 or more seismograms.

The major global discontinuities are seen at average depths of about 415, 520 and 655 km. There is some leakage into adjacent depth slices from the histogram smoothing and also from discontinuity topography. Owing to the long periods of these waveforms, reflectors can only be seen if they are more than about 80 km away from the surface or a major discontinuity. The upper discontinuities are bracketed by negative sidelobe artefacts (see, for example, the open circles for the 370 km depth slice). Owing to the limited bandwidth of the data, the cross-correlation procedure tends to identify negative peaks adjacent to the positively correlated main peaks. Although conceivably some of the negative values shown in Fig. 7 result from negative impedance contrast reflectors (e.g. the top of low-velocity zones), the vast majority undoubtedly result from sidelobe artefacts. In future work, it may be possible to reduce the size of these artefacts through deconvolution or using broader band data.

The main purpose of Fig. 18 is not to image the major discontinuities (which were discussed earlier), but to explore

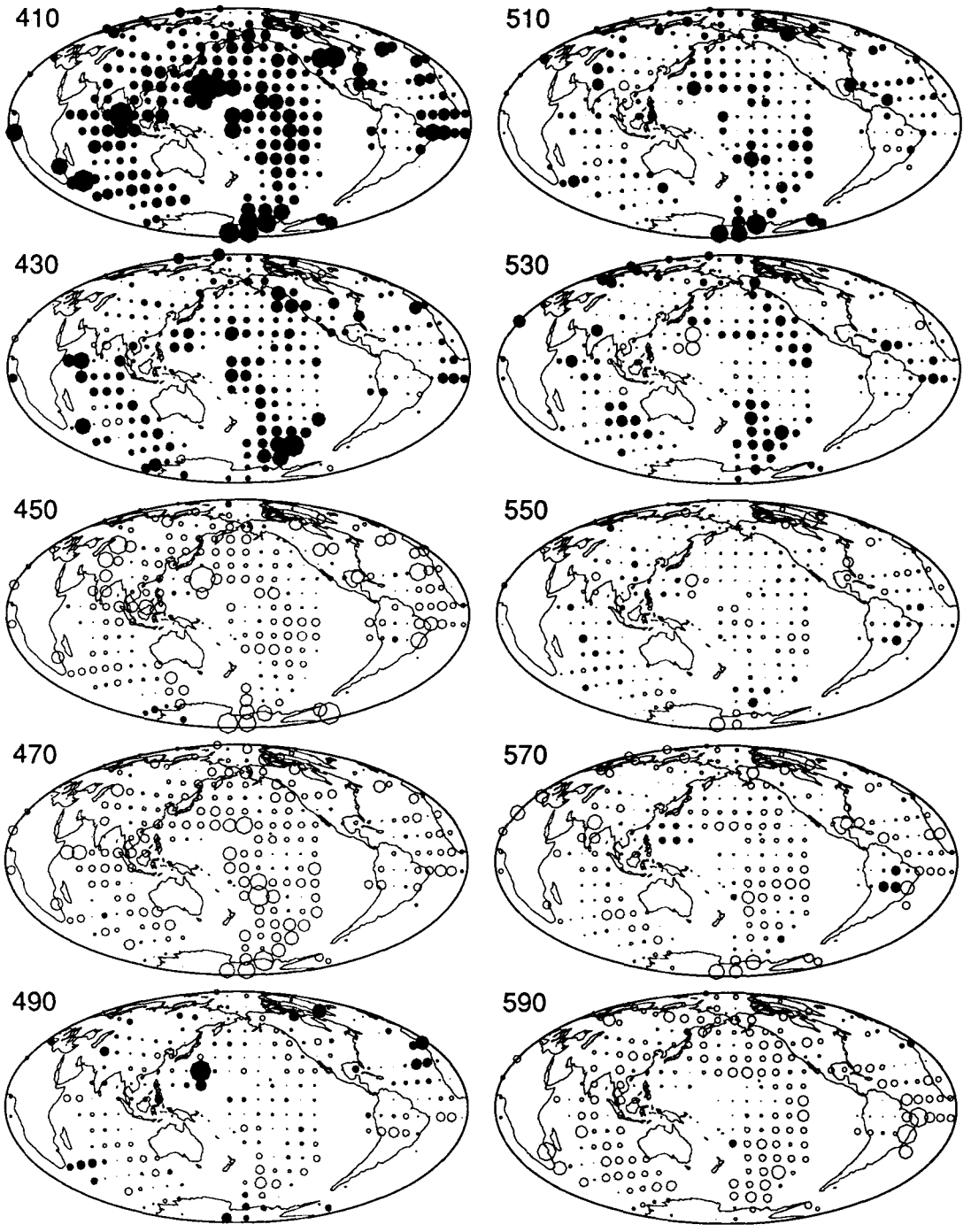

Figure 18. (*Continued.*)

the possible presence of additional reflectors at other depths. A peak found on a single histogram is not very convincing, but when a feature is seen in several adjacent caps it is more likely to be real. Caps which are greater than 10° apart do not share any seismograms in common and so represent independent samples. Many apparent reflectors, spanning three or more adjacent caps, are seen in Fig. 18, some of which appear nearly as strongly as the major reflectors. However, before accepting the reality of these features it is important to perform checks on their validity.

Our first check involves randomly scrambling the midpoint locations to the 5,884 seismograms involved in our analysis and then processing the data in the same way. Each cap average uses the same number of seismograms but the seismograms are a random selection from all of the available data, with midpoints that, in general, will scatter over the globe. The scrambling procedure is performed once for the entire data set; adjacent cells continue to share seismograms in common. Fig. 19 plots the resulting cap averages for depth slices between 210 and 390 km for caps with 20 or more seismograms. The anomalies seen within individual depth slices are entirely a result of random chance and

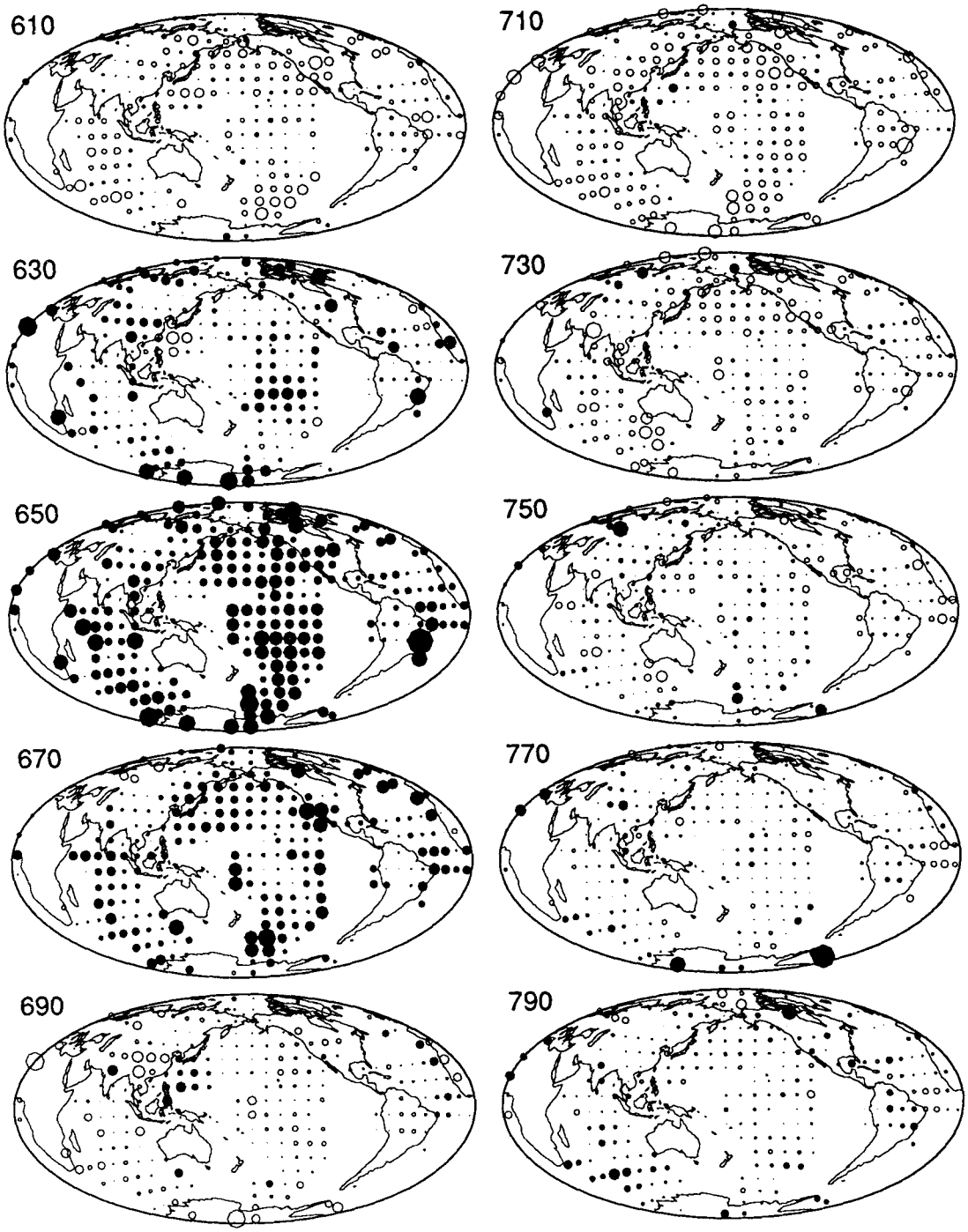

Figure 18. (*Continued.*)

cannot indicate actual earth structure. Examples of these anomalies include an apparent reflector at about 240 km beneath the Gulf of Mexico and a feature at about 310 km beneath South America. As one would expect, the anomalies tend to be largest for those caps with the smallest number of data, and the anomalies are not generally coherent beyond a few adjacent caps which have data in common.

Figure 19 shows that many of the smaller features seen at equivalent depths in Fig. 18 could be due to random chance. However, the larger anomalies in Fig. 18 appear to be statistically significant and often span larger areas than one would expect from pure chance. A disturbing aspect of Fig. 18 is that the anomalies tend to be largest in the caps with the fewest data. Caps containing 50 or more seismograms exhibit smaller anomalies. However, these smaller anomalies are still significantly larger than those predicted by random chance for caps with 50 or more traces.

Figure 19 suggests that the more prominent of the apparent reflectors seen above 400 km are unlikely to be a result of random fluctuations due to an inadequate number of data. However, this does not establish the reality of the

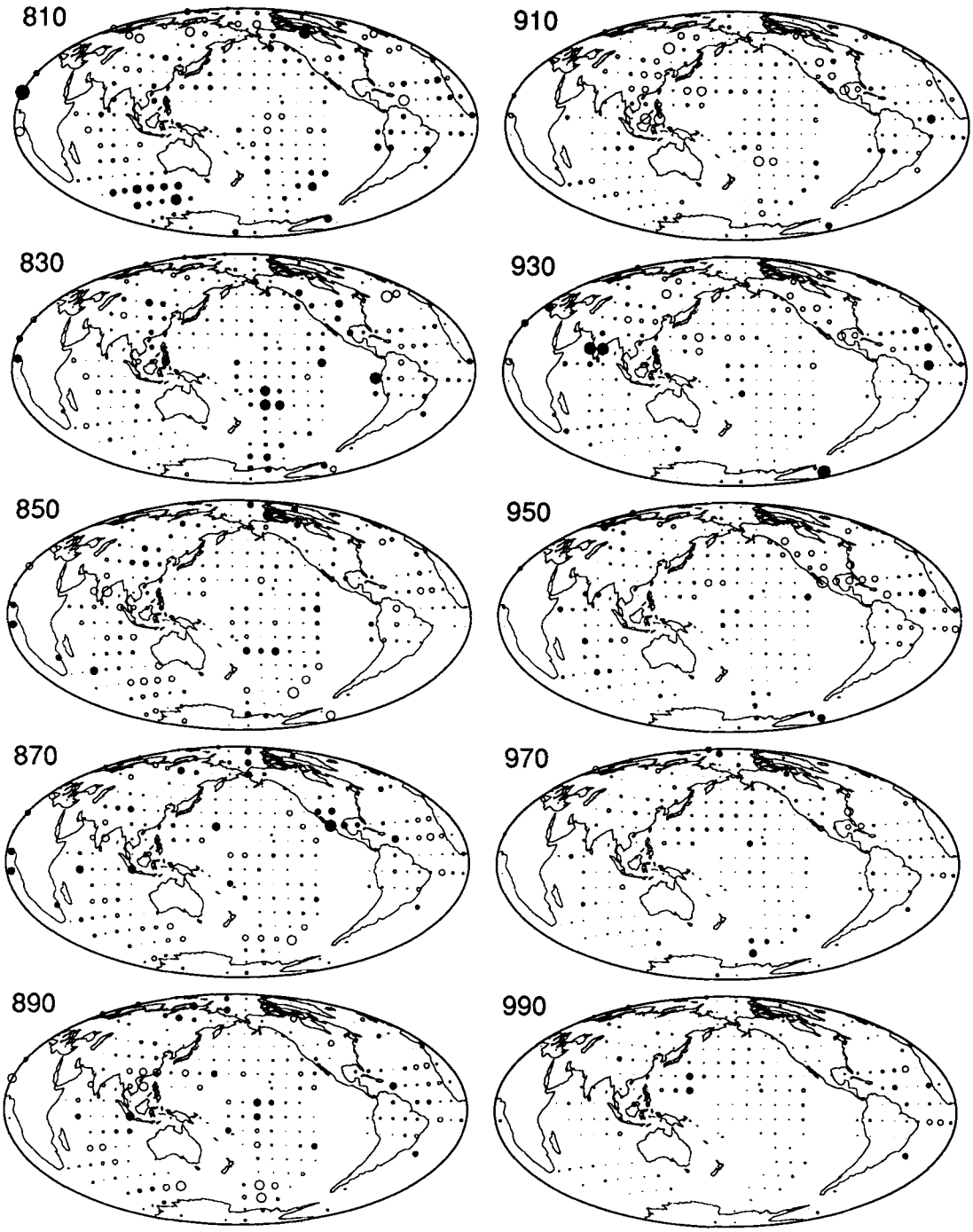

Figure 18. (*Continued.*)

reflectors, since seismograms within most caps have similar source and receiver regions and one could imagine sources of systematic noise which would cause apparent *SdS* arrivals. In order to test this possibility, we examined discontinuity depth histograms for selected caps which contained *SS* bounce points at different ray azimuths. The greatest variety of bounce-point azimuths are available in the northern Pacific. Fig. 20 shows bounce-point locations and azimuths in this area and the locations of seven caps which contain 50 or more seismograms in each of two distinct azimuth bins (50°–130° and 140°–220°). Fig. 21 plots histograms for these caps. If the shape of the depth histograms was entirely determined by discontinuity structure at the bounce points, we might expect to see very similar histograms for each azimuth grouping. However, agreement between the histograms outside the major discontinuity peaks is generally poor. This is unlikely to be due to differences in the positions of the bounce points within each cap since histograms from adjacent caps tend to be correlated.

The clear conclusion for these caps is that peaks above 410 km and below 660 km are not reliable features and

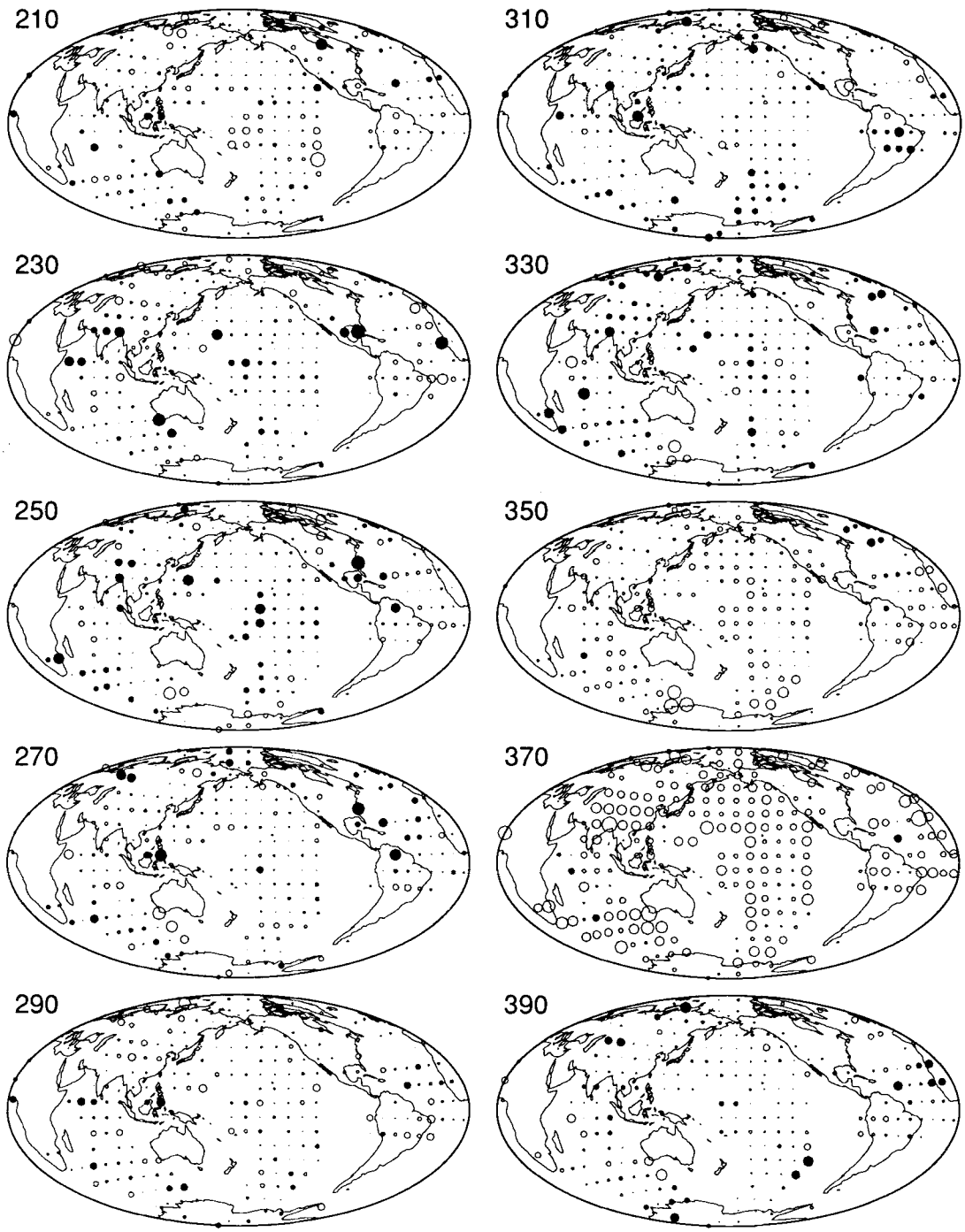

Figure 19. Histograms resulting from randomly scrambling the midpoint locations of the seismograms used in Figs 8 and 18. Each cap continues to contain the same number of seismograms.

should not be interpreted as indicating reflectors beneath the *SS* bouncepoints. This is not particularly surprising when one considers that no large anomalies are seen for these caps in the depth slices shown in Fig. 18, and the results of the random resampling test indicate that small peaks are to be expected due purely to chance. The possibility remains that the larger features seen in Fig. 18 are caused by discontinuity structure, but, unfortunately, these features typically are not defined by *SS* bounce points at a variety of azimuths. One exception is the apparent reflector at about 130 km depth beneath the Indian Ocean. Fig. 22 shows bounce-point locations and azimuths in this area and the locations of two caps which contain 20 or more seismograms in two azimuth bins. Histograms for these caps are plotted in Fig. 23. In this case there does appear to be some agreement in the peaks near 130 km. The offset in depths for the different azimuths within cap 271 could be a result of differences in the distributions of *SS* bounce points within

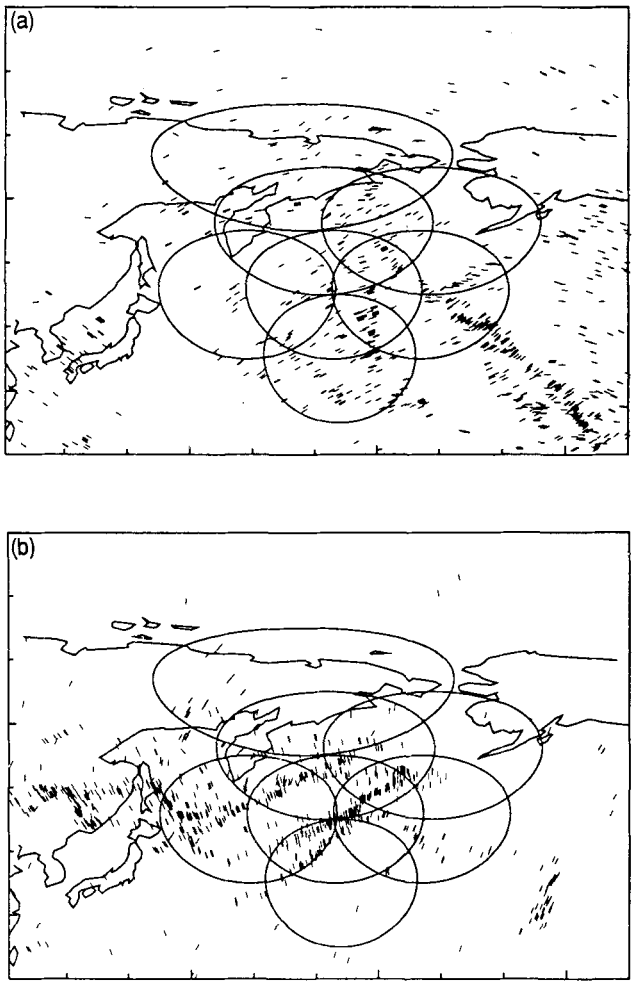

Figure 20. Northern Pacific *SS* bounce-point locations and local ray azimuths for (a) azimuths between 50° and 130°, and (b) azimuths between 140° and 220°. The perimeter of seven caps which contain over 50 seismograms in each azimuth grouping are also shown.

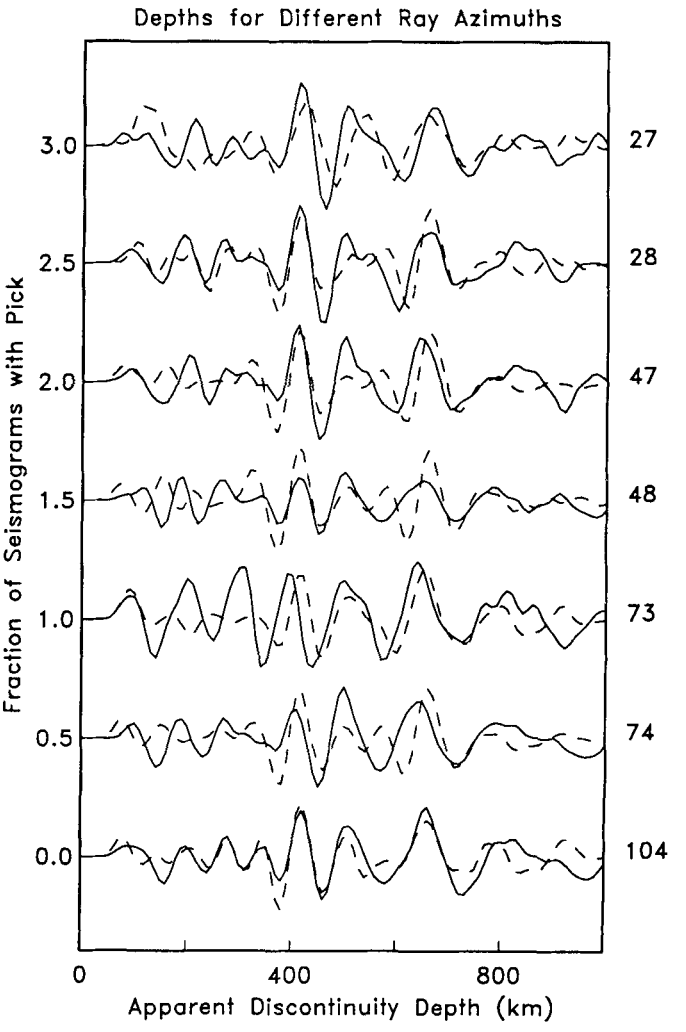

Figure 21. Histograms of discontinuity depths for the seven caps shown in Fig. 20 at azimuths between 50° and 130° (solid lines) and azimuths between 140° and 220° (dashed lines). Results from different caps are offset by 0.5 for clarity. Discontinuity depths are corrected for bounce-point topography and crustal thickness and mantle velocity model SH10C.

the cap and the reflector becoming more shallow to the east. Thus, there is some evidence that the apparent 130 km reflector beneath the Indian Ocean is real and not a result of structure near the sources or receivers. However, within these same caps, there is disagreement between the histograms regarding the presence of a reflector at about 310 km.

Do the apparent reflectors plotted in Fig. 18 show any agreement with previous models? Comparisons with the *ScS*-reverberation results of Revenaugh & Jordan (1991a) are in many respects the most relevant since the data and techniques used by Revenaugh & Jordan are similar to those used in this study. The *SS* bounce-point coverage is sparse in many of the regions sampled by Revenaugh & Jordan, but comparisons are possible to areas to the north of Australia. In some of these areas there is rough agreement in observed reflector depths, but overall there is no convincing evidence of a correlation between the Fig. 18 patterns and the reflectors obtained from the *ScS* reverberations. A more definitive comparison will be possible as data from many of the new global seismic stations become available and the *SS* bounce-point coverage improves (see below).

It is difficult to compare directly the *SS*-precursor results with the many regional and global tomography models for 3-D upper mantle *S*-wave structure, because the tomography models are usually expressed as smooth perturbations to a reference model. These perturbations are typically on the order of 5 per cent variations, which are large enough to cause long-period reflections if the velocity gradients were sufficiently steep (the reflection coefficient for 25 s shear waves falls off rapidly when the gradient region is thicker than about 25 km). However, in most cases, smoothness constraints imposed during the tomography-inversion procedure limit the sharpness of velocity changes in the models to longer scale lengths. Thus most tomography models do not predict long-period reflections except for the major discontinuities. It is probable, however, that models exist with much sharper velocity changes which are equally compatible with the data used in the tomographic studies.

There is, as yet, no clear answer regarding the believability of the larger features shown in Fig. 18 at depths outside the major discontinuities. However, the rapidly

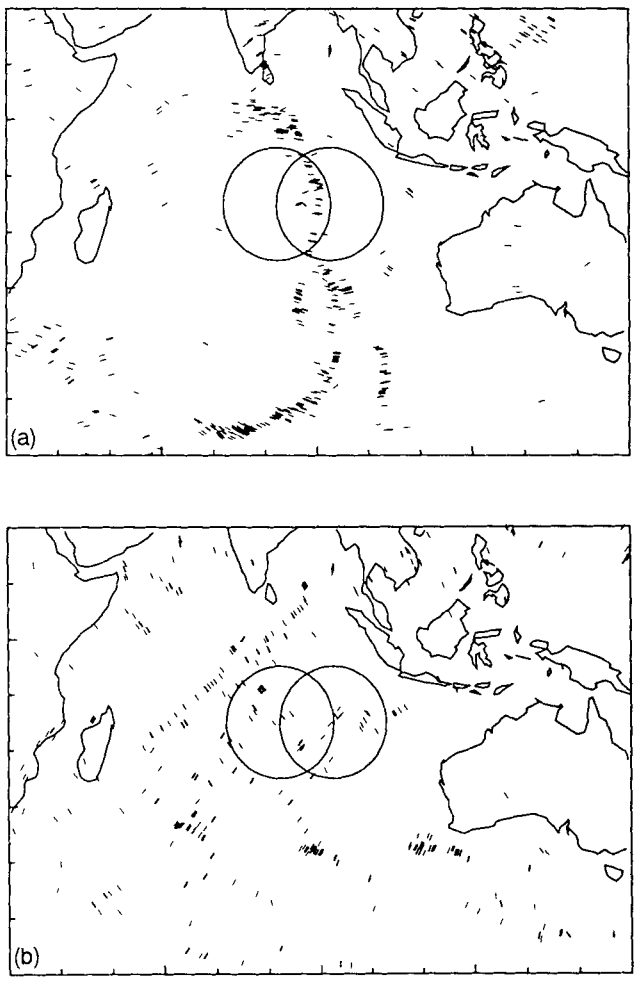

Figure 22. Indian Ocean *SS* bounce-point locations and local ray azimuths for (a) azimuths between 50° and 130°, and (b) azimuths between 140° and 220°. The perimeter of two caps which contain over 20 seismograms in each azimuth grouping are also shown.

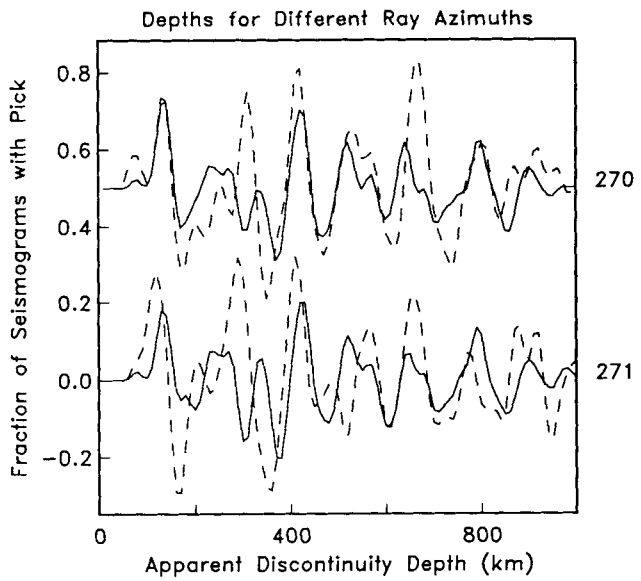

Figure 23. Histograms of discontinuity depths for the two caps shown in Fig. 22 at azimuths between 50° and 130° (solid lines) and azimuths between 140° and 220° (dashed lines). Results from different caps are offset by 0.5 for clarity. Discontinuity depths are corrected for bounce-point topography and crustal thickness and mantle velocity model SH10C.

improving distribution of global digital stations ensures that future analyses will give more definitive results. The increase in the number of seismograms will reduce the noise due to inadequate sampling, while the improved azimuthal coverage will permit better checks on the stability of the apparent reflectors. The simple histogram analysis presented here in which structure is assumed to occur only at the *SS* bounce point, while suitable for a preliminary analysis of the data, is too limited to account properly for the 3-D scattering effects. In principle, with suitable data coverage, techniques could be developed to 'migrate' the wavefield to account for off-axis scattering. The histogram technique is highly non-linear and does not preserve true amplitude information since only the times of possible *SdS* arrivals are used. It will be useful to experiment with stacks of the actual waveforms to see if similar results can be obtained.

The resolution of long-period data can be approximated by the size of the Fresnel zone. Fig. 24(a) plots the traveltime difference in seconds for deviations in the *SS* bounce-point position at 140° range. Note that the *SS* bounce point is a saddle point rather than a minimum time phase, consistent with the Hilbert transformed nature of this phase. For long-period GDSN data, the first Fresnel zone is approximated by the ±5 s contours in Fig. 24(a), a region about 15° across. It is also interesting to consider how a single point scatterer might appear in these data. Fig. 24(b) shows the apparent discontinuity depth as a function of position relative to a point scatterer at a depth of 350 km. It is analogous to the scattering hyperbola in reflection seismology, along which one would stack in order to migrate the data. An observation of such a pattern in the maps of apparent discontinuity depths would be an indication of a strong point scatterer in the earth (although no such pattern is clear in Fig. 18).

An ultimate goal of this research will be to directly invert the *SS* precursor waveforms for 3-D earth structure using a suitable synthetic-seismogram method. Finite difference modelling may be necessary to include fully the effects of diffraction and multiple scattering. It is conceivable that eventually every small wiggle between the major seismic phases in long-period data will be explained directly in terms of earth structure, rather than dismissed as noise or attributed to scattering from random heterogeneities which can only be described statistically.

ACKNOWLEDGMENTS

Guy Masters contributed valuable advice and many useful subroutines for this research. The availability of global digital data on CD-ROM from the United States Geological Survey greatly facilitated this project. This research was supported by National Science Foundation grant EAR91-18309.

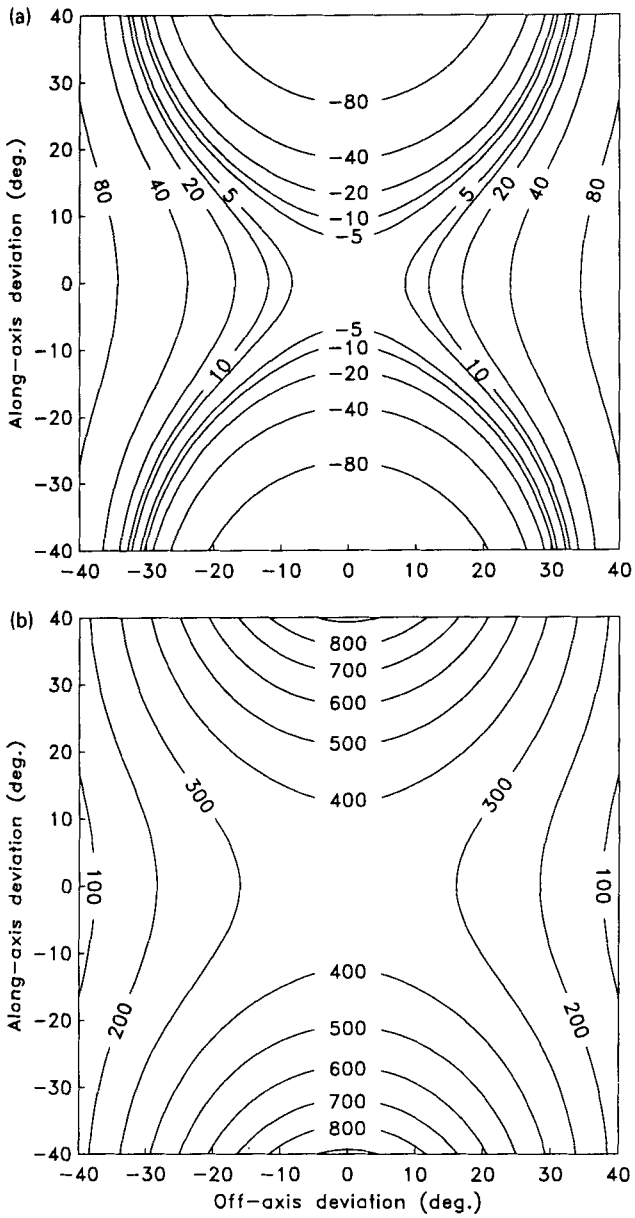

Figure 24. (a) The change in traveltime resulting from perturbations in the *SS* bounce-point position at a source-receiver range of 140°. The Fresnel zone for 20 s waves is given by the ±5 s contours. (b) Apparent discontinuity depth as a function of distance away from a single point scatterer at 350 km.

REFERENCES

Adams, R. D., 1971. Reflections from discontinuities beneath Antarctica, *Bull. seism. Soc. Am.*, **61**, 1441–1451.

Akaogi, M., Ito, E. & Navrotsky, A., 1989. Olivine-modified spinel–spinel transitions in the system Mg_2SiO_4–Fe_2SiO_4: calorimetric measurements, thermodynamic calculation, and geophysical application, *J. geophys. Res.*, **94**, 15671–15685.

Ashida, T., Kume, S. & Ito, E., 1987. Thermodynamic aspects of phase boundary among α-, β-, and γ-Mg_2SiO_4, in *High-Pressure Research in Mineral Physics*, pp. 269–274, ed Manghnani, M. H. & Syono, Y., Terra Scientific Publishing Company, Tokyo.

Barley, B. J., Hudson, J. A. & Douglas, A., 1982. *S*-to-*P* scattering at the 650 km discontinuity, *Geophys. J. R. astr. Soc.*, **69**, 159–172.

Baumgardt, D. R. & Alexander, S. S., 1984. Structure of the mantle beaneath Montana LASA from analysis of long-period mode-converted phases, *Bull. seism. Soc. Am.*, **74**, 1683–1702.

Bock, G., 1988. *Sp* phases from the Australian upper mantle, *Geophys. J.*, **94**, 73–81.

Bock, G. & Ha, J., 1984. Short-period *S*–*P* conversion in the mantle at a depth near 700 km, *Geophys. J. R. astr. Soc.*, **77**, 593–615.

Bock, G. & Kind, R., 1991. A global study of *S*-to-*P* and *P*-to-*S* conversions from the upper mantle transition zone, *Geophys. J. Int.*, **107**, 117–129.

Davis, J. P., Kind, R. & Sacks, I. S., 1989. Precursors to *P'P'* re-examined using broad-band data, *Geophys. J. Int.*, **99**, 595–604.

Dey-Sarkar, S. K. & Wiggins, R. A., 1976. Upper mantle structure in western Canada, *J. geophys. Res.*, **81**, 3619–3632.

Drummond, B. J., Muirhead, K. J. & Hales, A. L., 1982. Evidence for a seismic discontinuity near 200 km depth under a continental margin, *Geophys. J. R. astr. Soc.*, **70**, 67–77.

Dziewonski, A. M. & Anderson, D. L., 1981. Preliminary reference Earth model, *Phys. Earth planet. Inter.*, **25**, 297–356.

Efron, B. & Tibshirani, R., 1991. Statistical data analysis in the computer age, *Science*, **253**, 390–395.

Engdahl, E. R. & Flinn, E. A., 1969. Seismic waves reflected from discontinuities within earth's upper mantle, *Science*, **163**, 177–179.

Faber, S. & Müller, G., 1980. *Sp* phases from the transition zone between the upper and lower mantle, *Bull. seism. Soc. Am.*, **70**, 487–508.

Faber, S. & Müller, G., 1984. Converted phases from the mantle transition zone observed at European stations, *J. Geophys.*, **54**, 183–194.

Fukao, Y., 1977. Upper mantle *P* structure on the ocean side of the Japan–Kurile arc, *Geophys. J. R. astr. Soc.*, **50**, 621–642.

Fukao, Y., Obayashi, M., Inoue, H. & Nenbai, M., 1992. Subducting slabs stagnant in the mantle transition zone, *J. geophys. Res.*, **97**, 4809–4822.

Given, J. W. & Helmberger, D. V., 1980. Upper mantle structure of northwestern Eurasia, *J. geophys. Res.*, **85**, 7183–7194.

Grand, S. P. & Helmberger, D. V., 1984. Upper mantle structure of northwestern Eurasia, *Geophys. J. R. astr. Soc.*, **76**, 399–438.

Graves, R. W. & Helmberger, D. V., 1988. Upper mantle cross section from Tonga to Newfoundland, *J. geophys. Res.*, **93**, 4701–4711.

Gutowski, P. R. & Kanasewich, E. R. 1974. Velocity spectral evidence of upper mantle discontinuities, *Geophys. J. R. astr. Doc.*, **36**, 21–32.

Hales, A. L., 1969. A seismic discontinuity in the lithosphere, *Earth planet. Sci. Lett.*, **7**, 44–46.

Hales, A. L., Muirhead, K. J. & Rynn, J. M. W., 1980. A compressional velocity distribution in the upper mantle, *Tectonophysics*, **63**, 309–348.

Helmberger, D. V. & Engen, G. R., 1974. Upper mantle shear structure, *J. geophys. Res.*, **79**, 4017–4028.

Helmberger, D. V. & Wiggins, R. A., 1971. Upper mantle structure of midwestern United States, *J. geophys. Res.*, **76**, 3229–3245.

Husebye, E. S., Haddon, R. A. W. & King, D. W., 1977. Precursors to *P'P'* and upper mantle discontinuities, *J. geophys.*, **43**, 535–543.

Ito, E. & Takahashi, E., 1989. Postspinel transformations in the system Mg_2SiO_4–Fe_2SiO_4 and some geophysical implications, *J. geophys. Res.*, **94**, 10637–10646.

Ito, E. & Yamada, H., 1982. Stability relations of silicate spinels, ilmenites, and perovskites in *High-Pressure Research in*

Mineral Physics, pp. 405–419, Akimoto, S. & Manghnani, M. H., Center for Academic Publications, Tokyo.

Ito, E., Akaogi, M., Topor, L. & Navrotsky, A., 1990. Negative pressure-temperature slopes for reactions forming $MgSiO_3$ perovskite from calorimetry, *Science*, **249**, 1275–1278.

Johnson, L. R., 1967. Array measurements of *P* velocities in the upper mantle, *J. geophys. Res.*, **72**, 6309–6325.

Kanamori, H. & Press, F., 1970. How thick is the lithosphere?, *Nature*, **226**, 330–331.

Katsura, T. & Ito, E., 1989. The system Mg_2SiO_4–Fe_2SiO_4 at high pressures and temperatures: precise determination of stabilities of olivine, modified spinel, and spinel, *J. geophys. Res.*, **94**, 15663–15670.

Kennett, B. L. N. (ed.), 1991. *IASPEI 1991 Seismological Tables*, Research School of Earth Sciences, Australian National University, Canberra.

Kind, R. & Vinnik, L. P., 1988. The upper-mantle discontinuities underneath the GRF array from *P*-to-*S* converted phases, *J. Geophys.*, **62**, 138–147.

LeFevre, L. V. & Helmberger, D. V., 1989. Upper mantle *P*-velocity structure of the Canadian shield, *J. geophys. Res.*, **94**, 17749–17765.

Leven, J. H., Jackson, I. & Ringwood, A. E., 1981. Upper mantle seismic anisotropy and lithospheric decoupling, *Nature*, **289**, 234–239.

Masters, G. & Bolton, H., 1991. Large-scale shear velocity structure of the mantle, *EOS Trans. Am. geophys. Un.*, **72**, 316.

Masters, G., Jordan, T. H., Silver, P. G. & Gilbert, F., 1982. Aspherical Earth structure from fundamental spheroidal mode data, *Nature*, **298**, 609–613.

Nakanishi, I., 1986. Seismic reflections from the upper mantle discontinuities beneath the Mid-Atlantic ridge observed by a seismic array in Hokkaido region, Japan, *Geophys. Res. Lett.*, **13**, 1458–1461.

Nakanishi, I., 1988. Reflections of *P'P'* from upper mantle discontinuities beneath the Mid-Atlantic Ridge, *Geophys. J.*, **93**, 335–346.

Nakanishi, I., 1989. A search for topography of the mantle discontinuities from precursors to *P'P'*, *J. Phys. Earth*, **37**, 297–301.

Niazi, M., 1969. The use of source arrays in studies of regional structure, *Bull. seism. Soc. Am.*, **59**, 1631–1643.

Nolet, G., 1977. The upper mantle under western Europe inferred from the dispersion of Rayleigh modes, *J. Geophys.*, **43**, 265–285.

Paulssen, H., 1985. Upper mantle converted waves beneath the NARS array, *Geophys. Res. Lett.*, **12**, 709–712.

Paulssen, H., 1988. Evidence for a sharp 670-km discontinuity as inferred from *P*-to-*S* converted waves, *J. geophys. Res.*, **93**, 10489–10500.

Ram, A. & Mereu, R. F., 1977. Lateral variations in upper-mantle structure around India as obtained from Gauribidanur seismic array data, *Geophys. J. R. astr. Soc.*, **49**, 87–113.

Revenaugh, J. & Jordan, T. H., 1987. Observations of first-order mantle reverberations, *Bull. seism. Soc. Am.*, **77**, 1704–1717.

Revenaugh, J. & Jordan, T. H., 1989. A study of mantle layering beneath the western Pacific, *J. geophys. Res.*, **94**, 5787–5813.

Revenaugh, J. & Jordan, T. H., 1991a. Mantle layering from *ScS* reverberations: 2. the transition zone, *J. geophys. Res.*, **96**, 19763–19780.

Revenaugh, I. & Jordan, T. H., 1991b. Mantle layering from *ScS* reverberations: 3. the upper mantle, *J. geophys. Res.*, **96**, 19781–19810.

Richards, M. A. & Wicks, C. W., 1990. *S–P* conversion from the transition beneath Tonga and the nature of the 670 km discontinuity, *Geophys. J. Int.*, **101**, 1–35.

Sacks, I. S., Snoke, J. A. & Husebye, E. S., 1979. Lithosphere thickness beneath the Baltic Shield, *Tectonophysics*, **56**, 101–110.

Shearer, P. M., 1990. Seismic imaging of upper-mantle structure with new evidence for a 520-km discontinuity, *Nature*, **344**, 121–126.

Shearer, P. M. 1991. Constraints on upper mantle discontinuities from observations of long-period reflected and converted phases, *J. geophys. Res.*, **96**, 18147–18182.

Shearer, P. M. & Masters, T. G., 1992. Global mapping of topography on the 660-km discontinuity, *Nature*, **355**, 791–796.

Simpson, D. W., Mereu, R. F. & King, D. W., 1974. An array study of *P*-wave velocities in the upper mantle transition zone beneath northeastern Australia, *Bull. seism. Soc. Am.*, **64**, 1757–1788.

Souriau, A., 1986. First analyses of broadband records on the Geoscope network: potential for detailed studies of mantle discontinuities, *Geophys. Res. Lett.*, **13**, 1011–1014.

Stacey, F. D., 1977. *Physics of the Earth*, John Wiley and Sons, New York.

Stammler, K., Kind, R., Petersen, N., Kosarev, G., Vinnnik, L. & Qiyuan, L., 1992. The upper mantle discontinuities: correlated or anticorrelated?, *Geophys. Res. Lett.*, **19**, 1563–1566.

Stammler, K., Kind, R., Kosarev, G. L., Plesinger, A., Horalek, J., Qiyuan, L. & Vinnnik, L. P., 1991. Broadband observations of *PS* conversions from the upper mantle in Eurasia, *Geophys. J. Int.*, **105**, 801–804.

van der Hilst, R., Engdahl, R., Spakman, W. & Nolet, G., 1991. Tomographic imaging of subducted lithosphere below northwest Pacific island arcs, *Nature*, **353**, 37–43.

Vidale, J. E. & Benz, H. M., 1992. Upper-mantle seismic discontinuities and the thermal structure of subduction zones, *Nature*, **356**, 678–683.

Vinnik, L. P., 1977. Detection of waves converted from *P* to *SV* in the mantle, *Phys. Earth planet. Inter.*, **15**, 39–45.

Vinnik, L. P., Avetisjan, R. A. & Mikhailova, N. G., 1983. Heterogeneities in the mantle transition zone from observations of *P*-to-*SV* converted waves, *Phys. Earth planet. Inter.*, **33**, 149–163.

Walck, M. C., 1984. The *P*-wave upper mantle structure beneath an active spreading centre: the Gulf of California, *Geophys. J. R. astr. Soc.*, **76**, 697–723.

Wallace, T. C. & Holt, W. E., 1988. The 670 km discontinuity and precursors to *P'P'*: implications for the sharpness of the boundary and its global extent, *EOS Trans. Am. geophys Un.*, **69**, 1333.

Whitcomb, J. H. & Anderson, D. L., 1970. Reflections of *P'P'* seismic waves from discontinuities in the mantle, *J. geophys. Res.*, **75**, 5713–5728.

Wiggins, R. A. & Helmberger, D. V., 1978. Upper mantle structure of the western United States, *J. geophys. Res.*, **78**, 1870–1880.

Woodhouse, J. H. & Dziewonski, A. M., 1984. Mapping the upper mantle: three dimensional modeling of Earth structure by inversion of seismic waveforms, *J. geophys. Res.*, **89**, 5953–5986.

Woodward, R. L. & Masters, G., 1991. Global upper mantle structure from long-period differential travel times. *J. geophys. Res.*, **96**, 6351–6377.

Woodward, R. L. & Masters, G., 1992. Upper mantle structure from long-period differential times and free oscillation data, *Geophys. J. Int.*, **109**, 275–293.

Woodward, R. L., Forte, A. M., Su, W.-J. & Dziewonski, A. M., 1993. Constraints on the large-scale structure of the Earth's mantle, in *Evolution of the Earth and Planets, Am. geophys. Un., Monogr.* **74**, 89–109, Washington, DC.

Zhang, Z. & Lay, T., 1993. Investigation of upper mantle discontinuities near northwestern Pacific subduction zones using precursors to *sSH*, *J. geophys. Res.*, **98**, 4389–4405.